90

ORNL-4114
UC-34 – Physics

SYSTEM RESPONSE FUNCTIONS FOR FLIGHT-TIME SPECTROMETRY OF SECONDARY FAST NEUTRONS

(THESIS)

Robert T. Santoro

GPO PRICE $ ____
CFSTI PRICE(S) $ ____
Hard copy (HC) 3.00
Microfiche (MF) .65

N67-[illegible]
(ACCESSION NUMBER)
122
(PAGES)
CR-87805
(NASA CR OR TMX OR AD NUMBER)
(THRU)
1
(CODE)
24
(CATEGORY)
FACILITY FORM 602

OAK RIDGE NATIONAL LABORATORY
operated by
UNION CARBIDE CORPORATION
for the
U.S. ATOMIC ENERGY COMMISSION

Printed in the United States of America. Available from Clearinghouse for Federal
Scientific and Technical Information, National Bureau of Standards,
U.S. Department of Commerce, Springfield, Virginia 22151
Price: Printed Copy $3.00; Microfiche $0.65

ORNL-4114

Contract No. W-7405-eng-26

Neutron Physics Division

SYSTEM RESPONSE FUNCTIONS FOR FLIGHT-TIME SPECTROMETRY OF SECONDARY FAST NEUTRONS*

Robert T. Santoro

NOTE:
This Work Supported by
NATIONAL AERONAUTICS AND SPACE ADMINISTRATION
Under Order R-104(1)

*Presented to the Graduate Council of the University of Tennessee in partial fulfillment of the requirements for the degree of Master of Science.

AUGUST 1967

OAK RIDGE NATIONAL LABORATORY
Oak Ridge, Tennessee
operated by
UNION CARBIDE CORPORATION
for the
U. S. ATOMIC ENERGY COMMISSION

PRECEDING PAGE BLANK NOT FILMED.

TABLE OF CONTENTS

CHAPTER PAGE

LIST OF TABLES

LIST OF FIGURES

FIGURE PAGE

FIGURE PAGE

NOMENCLATURE

A_D = area of the detector face.

$A_k(t_m)$ = time analyzer response function (p. 60).

$B(\ell_p, \vec{\Omega})$ = distribution function for proton interactions (p. 36).

c = velocity of light in vacuum (cm./nsec.).

$C(v_p; v_n, t_i)$ = the jitter-smeared flight-time distribution function (p. 38).

D = detector thickness (cm.).

E_N = neutron energy (MeV.).

E_p = proton energy (MeV.).

$E_{\alpha max}$, $E_{\alpha min}$ = maximum and minimum possible α-particle energy values.

$E_\theta(t, \ell_p, x, v_n)$ = the detector geometric response function (p. 32).

$G(v_p; v_n, t)$ = the physical flight-time distribution function for detected neutrons (p. 31).

$\hat{i}, \hat{j}, \hat{k}, \hat{i}', \hat{j}', \hat{k}'$ = unit vectors in the x-y-z and x′-y′-z′ coordinate systems.

$J(t_j)$ = the instrumental time-jitter distribution function (p. 38).

k = time analyzer channel number.

K = index of refraction of the neutron detector scintillator.

$\vec{L}$ = normal distance from the x-y-z origin to the face of the detector (cm.).

ℓ_p = the distance from where the proton intersects the face of the target to the point of interaction in the target at $P_T(x,y,z)$, (cm.).

ℓ_f = the distance from $P_T(x,y,z)$ to a point on the flat face of the detector, $P_D(x' = 0, y', z')$, (cm.).

$\ell_D(t)$ = the pathlength travelled by the neutron in the detector expressed in terms of the apparent flight time (cm.).

ℓ_c = the normal distance from the neutron detection point to the phototube cathode (cm.).

ℓ_T = the pathlength travelled by the neutron in the target (cm.).

n = the conversion gain of the time analyzer (nsec. per channel).

$N(y,z)$ = proton beam distribution function (p. 32).

N_H, N_c = the atomic densities of hydrogen and carbon in the neutron detector scintillator.

R_D = detector radius (cm.).

R_T = target radius (cm.).

S = the target thickness along the beam axis, ($S = T \sec \psi$) (cm.).

$S_k(v_p;v_n,\theta)$ = the time-channel response function.

T = target thickness (cm.).

t_m = the measured flight time (nsec.).

t = the total physical flight time (nsec.).

$t_w(h)$ = the pulse-height dependent time slewing introduced by the detector (nsec.).

t_j = the time jitter of the apparatus (nsec.).

t_p = the interval from the time zero defined above to the (p,n) interaction point in the target, (nsec.).

t_n = the flight time between the birth and detection points for the neutron (nsec.).

t_c = the time required for light to travel from the neutron detection point to the cathode of the phototube (nsec.).

v_n = neutron velocity (cm./nsec.).

v_p = proton velocity (cm./nsec.).

$W[t_w(h),v_n]$ = the time-slewing response function (p. 44).

$x\text{-}y\text{-}z$ = beam coordinate system.

$x'\text{-}y'\text{-}z'$ = detector coordinate system.

α,ρ = cylindrical coordinate of the detector face.

ϵ_D = detector efficiency.

η_D = spectrometer efficiency.

θ = the angle between the x-axis and $\vec{L}$; the detector rotation angle.

$\xi\text{-}\eta\text{-}\zeta$ = the target coordinate system.

$\Sigma_p(v_p;v_n,\theta)$ = differential macroscopic neutron production cross section (cm.$^{-1}$).

$\Sigma(v_n)$ = macroscopic "efficiency" cross section for neutron detection (cm.$^{-1}$).

Σ_D^{eff} = effective macroscopic absorption cross section for neutrons in the detector (cm.$^{-1}$).

Σ_{TN}^{eff} = effective macroscopic absorption cross section for neutrons in the target (cm.$^{-1}$).

Σ_{TP}^{eff} = effective macroscopic cross section for proton absorption in the target (cm.$^{-1}$).

$\Sigma_H(E_N,E_p)$ = differential macroscopic cross section for elastic scattering of neutrons of energy E_N in hydrogen (cm.$^{-1}$).

$\Sigma_c(n,\alpha)$ = differential macroscopic cross section for the production of alpha particles (cm.$^{-1}$).

Σ_c^{eff} = effective macroscopic cross section for the cascade reaction (cm.$^{-1}$).

σ_α = total microscopic cross section for the $^{12}C(n,\alpha)^{9}Be$ reaction.

$\sigma_{c,ne}$ = nonelastic microscopic cross section for carbon.

σ_N = microscopic total cross section for hydrogen.

σ = standard derivation of the proton beam distribution about the y-z plane.

σ_y' = $1.18\sigma \sec \Psi$, the effective target radius used in the maximum flight-time uncertainty calculations.

σ_j = the standard derivation of the time jitter distribution.

Ψ = the target rotation angle, $|\Psi| \le \pi/2$.

τ_2, τ_1 = elements of target thickness measured along $\pm\xi$. $(\tau_1 \le \xi \le \tau_2)$.

$\vec{\Omega}$ = neutron direction from $P_T(x,y,z)$ to $P_D(x' = 0,y',z')$.

ACKNOWLEDGMENTS

The author wishes to thank the Oak Ridge National Laboratory, operated by Union Carbide Corporation for the Atomic Energy Commission for providing the opportunity and facilities for doing this thesis and the National Aeronautics and Space Administration for supporting the research.

The author is particularly grateful to R. W. Peelle for suggesting this problem and for his patience, encouragement, and advice in the formulation and execution of all phases of the thesis. Thanks are also due W. Zobel and J. W. Wachter for their help and comments in the writing and organization of the computer programs.

Thanks are also extended to Miss Lenna Lovette for typing the manuscript.

ABSTRACT

Time-channel response functions have been derived for a time-of-flight spectrometer used to measure monoenergetic secondary neutrons in the energy region from 2 to 100 MeV. produced in homogeneous slab targets from the interactions of monoenergetic charged particles with the target nuclei. The effects on the flight-time distribution of the target and detector dimensions and orientation, the spatial distribution of the beam, and the pulse-height dependent time slewing (walk) were demonstrated. Response functions were derived assuming that the neutron emission from the target is independent of the azimuthal scattering angle and the polar angle over the angular region subtended by the detector, that neutron detection may be treated in the first collision approximation with the light being emitted uniformly from the interaction point and collected uniformly from all points in the detector volume, that the beam dimension perpendicular to the scattering plane can be ignored, and that the instrumental timing jitter can be approximated by a Gaussian distribution independent of the pulse height. The time-channel response functions were obtained from the integral over the time-analyzer response function of the convolution of the physical flight-time distribution of detected neutrons and the time-slewing response function. The maximum flight-time uncertainties, $\Delta t/t$, were derived in terms of the target and detector dimensions assuming that all dimensions have negligible effect except the one being evaluated. Comparisons are made between the computed distributions and those obtained analytically. The expected dominant effects of the detector thickness are demonstrated along with the dependence of the target dimensions on the neutron velocity and the angular difference between the neutron scattering angle and the target rotation angle. The distributions arising from the target and detector thickness were shown to be square except for attenuation effects, while those obtained for large detector radii showed a 1/t dependence. The time distribution for large beam size reflects the beam spatial distribution. The numerical methods are described, and typical distributions illustrate each contribution to the overall response function. Where multiple scattering does not dominate, the time integral of the computed response functions are in good agreement with known detector efficiencies.

CHAPTER I

INTRODUCTION

The determination of neutron energy by time-of-flight is one of the most direct methods for neutron spectroscopy. The method was originally conceived for measurements of neutrons in the electron volt energy region, but with the development of fast, highly efficient neutron detectors and improvements in pulse electronic instrumentation, measurements were extended into the region up to 20 MeV.[1-4] Recently, flight-time techniques have been used at even higher energies to measure target yields and differential cross sections for the interactions of 50- to 150-MeV. protons with nuclei.[5]

Experiments have been performed at the Harvard Synchrocyclotron using time-of-flight techniques to measure the differential cross sections for the production of neutrons resulting from the interactions of 160-MeV. protons with target nuclei.[6] As part of the analysis of these data, this study was initiated to determine the time response function

---

[1] F. G. J. Perey, Inelastic Scattering of 14-MeV. Neutrons in Carbon, Oxygen, and Lithium, Ph.D. dissertation, University of Montreal, 1960.

[2] G. K. O'Neill, Phys. Rev. 95, 1235 (1954).

[3] A. Adam, G. Palla, and P. Quittner, Acta. Phys. Hung. Tom. XVII Fasc. 3, 1964.

[4] J. Rethneiv et al., Nucl. Inst. Methods 17, 273 (1962).

[5] P. H. Bowen et al., Nucl. Phys. 30, 475 (1962).

[6] R. W. Peelle et al., Neutron Phys. Div. Ann. Progr. Rept. Sept. 1, 1962, ORNL-3360, p. 286.

for monoenergetic neutrons in the range 2 to 100 MeV. in the experimental geometry.

I. A SIMPLIFIED FLIGHT-TIME SPECTROMETER

Figure 1 shows a simplified time-of-flight spectrometer based on the one described by Peelle et al.[7] The flight-time of the neutron is inferred from the time interval between the pulse produced in the zero-time detector by the incident proton and the pulse from the disc-shaped NE-213[8] neutron detector. (Not shown in the diagram are the additional detectors and instrumentation for charged-particle and gamma-ray discrimination since it is assumed that only neutrons interact in the neutron counter.) A scintillating detector is shown as the zero-time detector; however, such devices as induction electrodes or the rf signal from the proton accelerator may be used. In some applications, the alpha or gamma radiation accompanying the formation of the neutron is detected by a counter located near the target to provide the zero-time signal. The conversion gain of the time analyzer is 0.500 nsec./channel.

II. REVIEW OF NEUTRON FLIGHT-TIME SPECTROSCOPY

The resolution of a time-of-flight spectrometer is determined for a given neutron energy from the flight-time interval measurement

---

[7] R. W. Peelle et al., Differential Cross Sections for the Production of Protons in the Reactions of 160-MeV Protons on Complex Nuclei, ORNL-3887, September 1966.

[8] NE-213 is a liquid scintillator manufactured by Nuclear Enterprises, Ltd., Winnipeg, Canada.

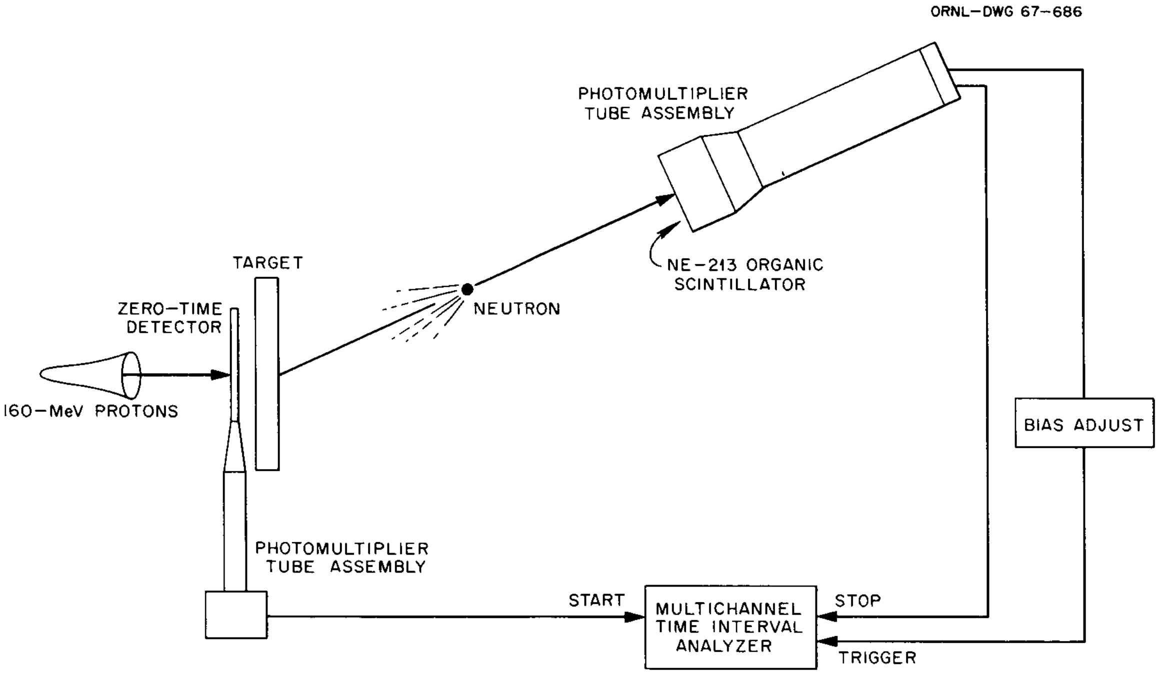

Figure 1. Simplified block diagram of the neutron time-of-flight spectrometer.

uncertainty combined with the uncertainty in the flight path.[9] The timing uncertainty is the combination of the partial uncertainties arising from the scintillator detector, photomultiplier tubes, timing circuits, and time analyzer channel width. The flight-path uncertainty is introduced by the variation in the birth and detection points within the target and detector. The relative uncertainty in the measurement of the energy is twice as large as the combination of all geometric and timing uncertainties. To achieve optimum energy resolution, the dominant contributions must be controlled.

A detailed discussion of time-of-flight techniques is given by Neiler and Good.[10] They separate the instrumental resolving time into three "measurable" functions; the uncertainty in the time-of-origin of the neutron, the geometry of the detecting medium, and the uncertainties associated with detection and electronic processes. Each of these factors requires special consideration by the experimenter. Rybakov and Siderov[11] point out the improved resolving power is, in general, obtained by increasing the flight path. This idealization is not always practical since the loss in counting rate with distance and the signal to background ratio for available beam intensity may require short flight paths. Additionally, scattering from the floor and walls of the experimental area

---

[9] The uncertainty is defined here as the predictable spread in values for a given measurement and not the unknown systematic error in the mean of the resulting distribution.

[10] J. H. Neiler and W. M. Good, Fast Neutron Physics, (Interscience Publishers, New York, 1963), pp. 509-621.

[11] B. V. Rybakov and V. A. Siderov, Fast Neutron Spectroscopy, (Consultants Bureau, Inc., New York, 1960), pp. 101-109.

requires more complicated apparatus when using long flight paths, because of the possibility of detecting neutrons degraded in energy.

Brooks[12] lists four criteria for selecting a detector for flight-time measurements. These are: time-resolution, detector efficiency, discrimination against background, and physical considerations, e. g., thickness and/or area. The timing resolution that can be achieved depends on the choice of the scintillator and photomultiplier tube. The large amplitude range in the light output from the detection event causes a portion of the amplitude spread to be translated into time spread by the electronics normally called time walk or slewing. Additionally, the statistical nature of the cathode photoelectron emission and electron multiplier introduce timing fluctuation or jitter. As Lundby[13] has shown, the construction of the scintillator-phototube assembly must also be considered. Detailed studies of the timing resolution have been made by Colombo, Gatti, and Pignanelli[14] who have related the resolving time to the variance of the centroid of the current pulse from the phototube and the pulse-height dependent time-slewing. Graphic results have also been presented by Gatti and Svelto[15] for estimating the time resolution for given bias levels as a function of the scintillator decay time constant and statistical properties of the phototube specified by the

---

[12] F. D. Brooks, Proc. Symp. on Neutron Time-of-Flight Methods, Saclay (1961), p. 403.

[13] A. Lundby, Rev. Sci. Instr. 22, 324 (1951).

[14] S. Colombo, F. Gatti, and M. Pignanelli, Nuovo Cimento 5, 1739 (1957).

[15] E. Gatti and V. Svelto, Nucl. Inst. and Methods 30, 213 (1964).

transit time fluctuations. Several methods of time measurement and their associated relative timing errors are discussed in detail by Neiler and Good and Rybakov and Siderov.

At neutron energies over 0.5 MeV., detection is usually accomplished with n-p scattering using organic scintillators. Organic scintillators are characterized by fast decay times and relatively high efficiency. Birks[16] has investigated the basic processes of scintillation and has derived analytic relationships between the fast and slow light components of the decay process while Batchelor et al.[17] and Verbinski et al.[18] have separately measured the response functions of organic scintillators for fast neutrons and have established the relationships between the light output and the energy for electrons, protons, alpha particles, and carbon recoils. Analytic methods for determining the detection efficiency of organic phosphors to neutrons in the energy region below 20 MeV. have been suggested by Kurz[19] and by Schuttler[20] and absolute efficiency values have been reported by Love and his coworkers.[21]

---

[16] J. B. Birks, IRE Transactions on Nuclear Science, NS-7, 2 (1960).

[17] R. Batchelor et al., Nucl. Instr. Methods 13, 20 (1962).

[18] V. V. Verbinski et al., The Response of Some Organic Scintillators to Fast Neutrons, Shielding Division Report, ANS-SD-2, December 1964.

[19] R. J. Kurz, A 709/7090 Fortran II Program to Compute the Neutron-Detection Efficiency of Plastic Scintillator for Neutron Energies From 1 to 300 MeV., UCRL-11339, March 1964.

[20] R. S. Schuttler, Efficiency of Organic Scintillators to Fast Neutrons, ORNL-3888, July 1966.

[21] T. A. Love et al., Absolute Efficiency Measurements of NE-213 Organic Phosphors for Detecting 14.4- and 2.6-MeV. Neutrons, ORNL-3893, September 1966.

Recalling the detector criteria of Brooks, one must finally consider the physical dimensions of the detector. For thin detectors in which the attenuation is minimal, the efficiency is proportional to the detector thickness. For detectors of thicknesses comparable to the fast neutron mean free path, the proportionality breaks down, e. g., 7 cm. at 2 MeV. Grismore and Parkinson[22] have investigated the relationship between the resolving power and the neutron energy for flight paths of 5.3 and 15 m. and detector thicknesses of 2 and 8 cm. They have shown that for 6-MeV. neutrons produced by $^{16}O(d,n)$ reactions and 3 nsec. time resolution, the geometric factors which limit the resolving power are just equal to the time resolution when a 6-cm. detector and a 5-cm. thick gas target are used. Rybakov and Siderov give graphic results for the neutron energy and flight distance required to obtained 3% and 1% energy resolution for a 5-cm. thick detector for $\Delta t = 3$ nsec.

Typical factors which determine the resolution time have been summarized in a paper by Smith[23] for a time-of-flight spectrometer used to study neutrons with energies between 2 and 4 MeV.

III. PURPOSE OF THE THESIS AND PROPOSED WORK

The purpose of this thesis is to calculate the expected neutron flight-time distributions for monoenergetic neutrons resulting from the bombardment of homogeneous targets by monoenergetic protons and to study

---

[22] R. Grismore and W. C. Parkinson, Rev. Sci. Instr. 28, 245 (1957).

[23] R. V. Smith, Conference on Neutron Physics by Time-of-Flight, Gatlinburg, Tennessee, 1956, p. 103.

the behavior of these distributions for variations in the geometric parameters of the beam, target, and detector.

Several restrictions have, however, been imposed on the design of the model spectrometer which is used as well as the physical phenomena leading to birth and detection of the neutrons:

1. The target and detector are right-circular cylinders mounted so that the particles first strike the flat surfaces.
2. The calculations are made for 160-MeV. protons whose specific energy loss in the target is approximated by its true value at the center of the target. Multiple scattering of the protons or secondary neutrons in the target is ignored. The proton density distribution is approximated either by a bivariate normal frequency function with a diameter much less than the target diameter, or as uniform over the target.
3. Neutron emission from the target is assumed independent of the azimuthal scattering angle, as well as independent of the polar angle over the angular range subtended by the detector. No interactions occur in the region between the target and detector.
4. Neutron detection is restricted to the first collision approximation and the resulting light is emitted from the interaction point and collected uniformly from all points in the detector volume. Light transit times are obtained from the normal distance to a flat photocathode with the scintillator coupled directly to the multiplier tube. Phototube delays are taken as independent of the position where the light strikes the photocathode.

5. Timing jitter was represented by a normal frequency function with standard deviation independent of pulse height from the scintillation detector.

For various secondary neutron energies the analysis will show the effects on the flight-time distribution of:

1. the angle between the beam direction and the target-detector axis,
2. the target thickness and orientation, including consideration of the energy loss of the incident protons,
3. the detector dimensions,
4. the spatial distribution of the proton beam,
5. the timing fluctuations between the flight time and the observed "machine" time, and
6. the time-slewing and analyzer response.

CHAPTER II

COORDINATE SYSTEMS

I. SPACE COORDINATES

Figure 2 shows the target and detector in the typical experimental configuration treated in the calculations which follow. A cartesian coordinate system, x-y-z, is constructed such that the positive direction of the x-axis is along the direction of the proton beam with the x-y plane containing the center of the detector and the target normal. The target coordinate system, ξ-η-ζ, is constructed so that the vertex of the ξ-η-ζ system is in conjunction with the origin of x-y-z with ξ and η constrained to rotate in the x-y plane and ξ along the target normal. The angle of rotation, Ψ, is limited to values defined by $|\Psi| < \pi/2$. The target thickness, T, is measured along ξ such that $\tau_2 - \tau_1 = T$ and

$$\tau_1 \leq \xi \leq \tau_2 \qquad \text{II-1}$$

for all values of ξ in the target.

The position of the neutron detector is given by $|\vec{L}| \equiv L$ and θ, where $\vec{L}$ is a vector in the x-y plane from the origin to the face of the detector and normal to it, and θ is the angle between the x-axis and $\vec{L}$.

The detector coordinate system, x'-y'-z', is constructed within the detector so that the origin of x'-y'-z' is at the terminus of $\vec{L}$ with the positive direction of the x'-axis along the axis of the detector.

ORNL-DWG 66-7305R

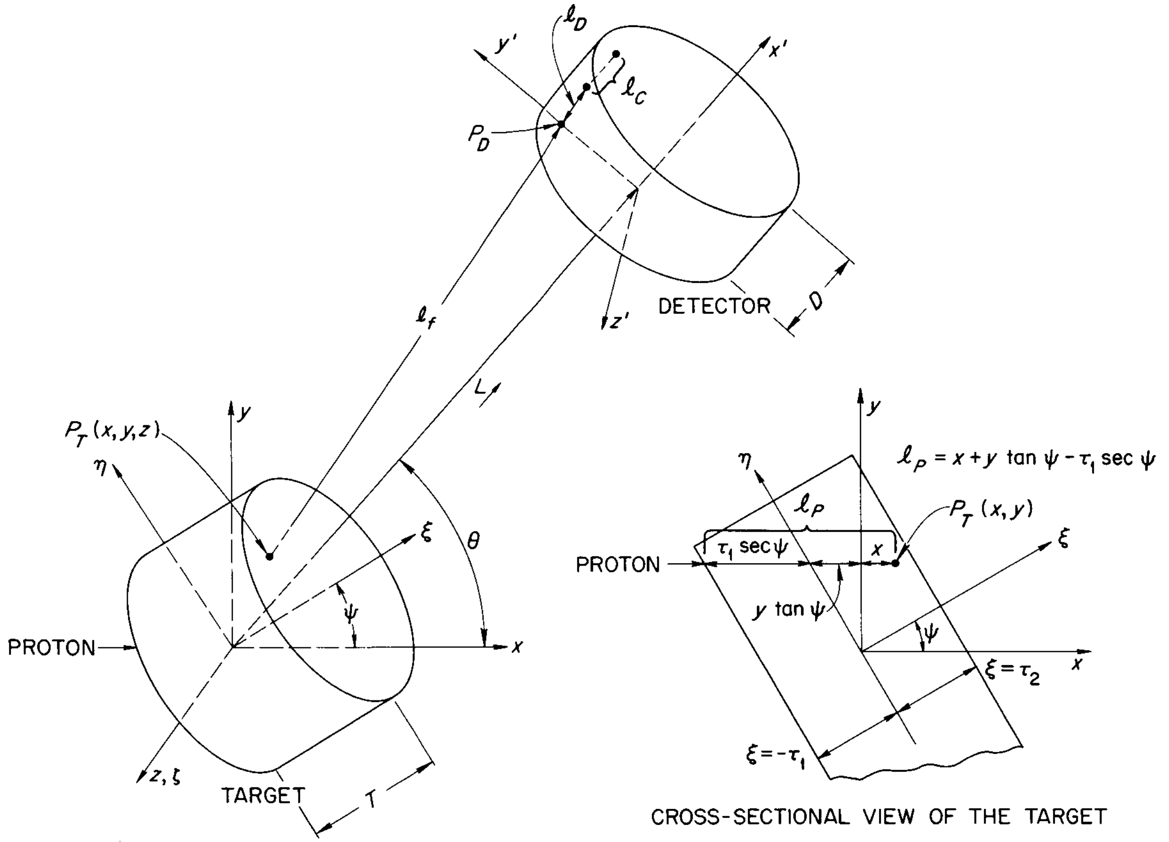

CROSS-SECTIONAL VIEW OF THE TARGET

Figure 2. The target and detector coordinate systems.

Transformation from the primed system to the unprimed system is accomplished using the expressions

$$\begin{aligned} x &= x' \cos\theta - y' \sin\theta + |\vec{L}| \\ y &= y' \cos\theta + x' \sin\theta \\ z &= z' \end{aligned} \qquad \text{II-2}$$

The distance from where the proton intersects the face of the target to the point of interaction in the target, $P_T(x,y,z,)$, is

$$\ell_p = x + y \tan\Psi - \tau_1 \sec\Psi \quad . \qquad \text{II-3}$$

ℓ_f is the distance from $P_T(x,y,z)$ to a point on the flat face of the detector, $P_D(x' = 0, y',z')$ and ℓ_D is the distance travelled by the neutron from $P_D(x' = 0, y',z')$ to the point of the nuclear reaction leading to detection. The light is considered to travel the normal distance ℓ_c from the detection point to the phototube cathode.

II. TIME COORDINATES

In this study, the arbitrary convention is adopted that the zero of time for a given incident proton is at the instant it would have passed through the plane x = 0 if the target were absent. Apparatus delays, including those of the phototube, are ignored. These conventions do not affect the generality of the results.

If n is the conversion gain of the time analyzer in nanoseconds per channel, then the measured flight time t_m for an event is recorded in channel k if

$$n(k - 1/2) < t_m \le n(k + 1/2) \quad . \qquad \text{II-4}$$

t_m is given by

$$t_m = t + t_w(h) + t_j = t_p + t_n + t_c + t_w(h) + t_j \qquad \text{II-5}$$

where

- t is the total physical flight time,
- $t_w(h)$ is the pulse-height dependent time slewing introduced by the detector,
- t_j is the time jitter of the apparatus,
- t_p is the interval from the time zero defined above to the (p,n) interaction point in the target,
- t_n is the flight time between the birth and detection points for the neutron,
- t_c is the time required for light to travel from the neutron detection point to the cathode of the phototube.

CHAPTER III

MAXIMUM FLIGHT-TIME UNCERTAINTIES

The time-of-flight of a neutron is related to the energy and the flight path in the nonrelativistic approximation by

$$t(\text{nsec.}) = \frac{72.3\ L(\text{meters})}{E_N^{1/2}\ (\text{MeV.})} \quad , \qquad \text{III-1}$$

and it follows directly that the relative resolution time for a given ΔL is simply $(\Delta t/t) = (\Delta L/L)$, where ΔL is introduced by the flight-path uncertainty between the birth and detection points within the target and detector. We shall calculate the maximum relative flight-time uncertainties $\Delta t/t$ in terms of the target and detector dimensions assuming that all dimensions have negligible effect except the one being evaluated; so that in the practical case the various effects would have to be combined. The convention will be adopted in which Δt is the difference between the maximum and minimum flight times while $t = L/v_n$, where L is the distance from the center of the target to the center of the detector face and v_n is the neutron velocity.

I. DETECTOR EFFECTS

For the detector geometry shown in inset A of Figure 3, in which the radius produces the dominant flight-path variation, the maximum and minimum neutron flight times are given by

ORNL-DWG 67-687

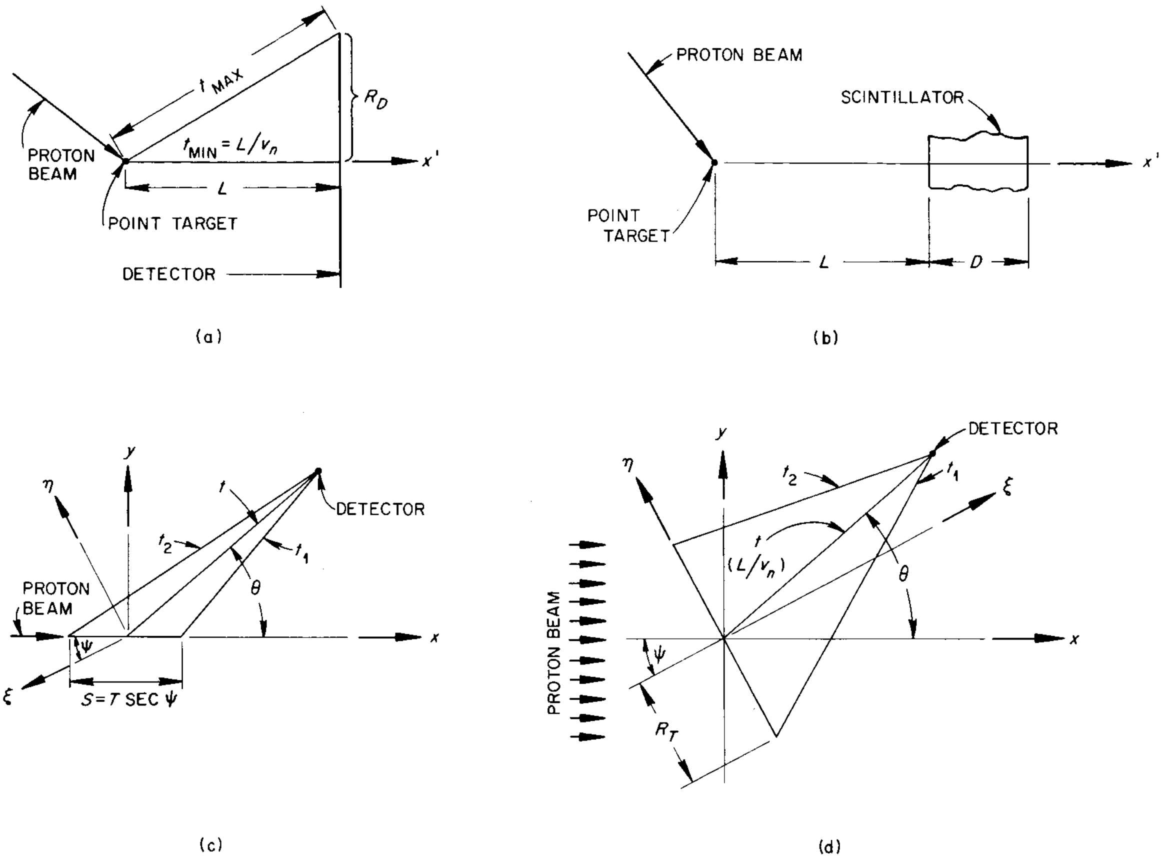

Figure 3. Detector and target geometries used in the maximum flight-time uncertainty calculations. In inset D, the proton beam uniformly illuminates the target.

$$t_{max} = \frac{1}{v_n}\left(L^2 + R_D^2\right)^{1/2} \qquad \text{III-2}$$

and

$$t_{min} = L/v_n \quad , \qquad \text{III-3}$$

where R_D is the detector radius. Expanding III-2 in a binomial series and subtracting III-3 yields the flight-time uncertainty Δt. Division by t gives the maximum flight-time resolution as

$$\left(\frac{\Delta t}{t}\right)_{R_D} = \frac{1}{2}\left(\frac{R_D}{L}\right)^2 \left(1 - \frac{1}{4}\frac{R_D^2}{L^2} + \dots\right) \quad . \qquad \text{III-4}$$

In typical applications, $R_D/L < 0.1$, and all terms beyond the first may be ignored since their total relative contribution to the resolution time is less than 10^{-5}.

Inset B of Figure 3 shows the geometry for a "thick" detector. Considering the effects of the detector thickness D, the maximum variation in the flight time is

$$\Delta t = \frac{D}{v_n} - \frac{KD}{c} \quad . \qquad \text{III-5}$$

The second term on the right-hand side of the equation gives the correction for the light transit time through the scintillator medium under the simplifying assumptions given in the introduction. K is the index of refraction of the scintillator and c is the velocity of light in vacuum. Dividing both sides of III-5 by the nominal flight time t we obtain the maximum flight time resolution for the axial dimension of the detector as

$$\left(\frac{\Delta t}{t}\right)_D = \frac{D}{L}\left(1 - \frac{Kv_n}{c}\right) \quad . \qquad \text{III-6}$$

Figure 4 shows the results of plotting the time resolution as a function of R_D/L and D/L. Equation III-6 is plotted for two values of v_n corresponding to 2- and 100-MeV. neutrons. These data show the expected dominant effect of the detector thickness.

It is interesting to note the relationship between R_D and D for a detector of constant volume and minimum relative flight-time uncertainty. The spectrometer efficiency η_D is given by the product of the detector efficiency, ϵ_D, and the solid angle subtended at the target by the detector. ϵ_D is defined here as the ratio of the number of neutrons detected to the total number of neutrons incident on the face of the detector. Ignoring attenuation in the scintillator, $\epsilon_D \simeq \Sigma(v_n)D$, where $\Sigma(v_n)$ is the macroscopic efficiency cross section for detection in the scintillator. Then,

$$\eta_D = \epsilon_D \cdot \frac{A_D}{L^2} \simeq \Sigma(v_n)D\frac{\pi R_D^2}{L^2} \qquad \text{III-7}$$

ORNL-DWG 67-688

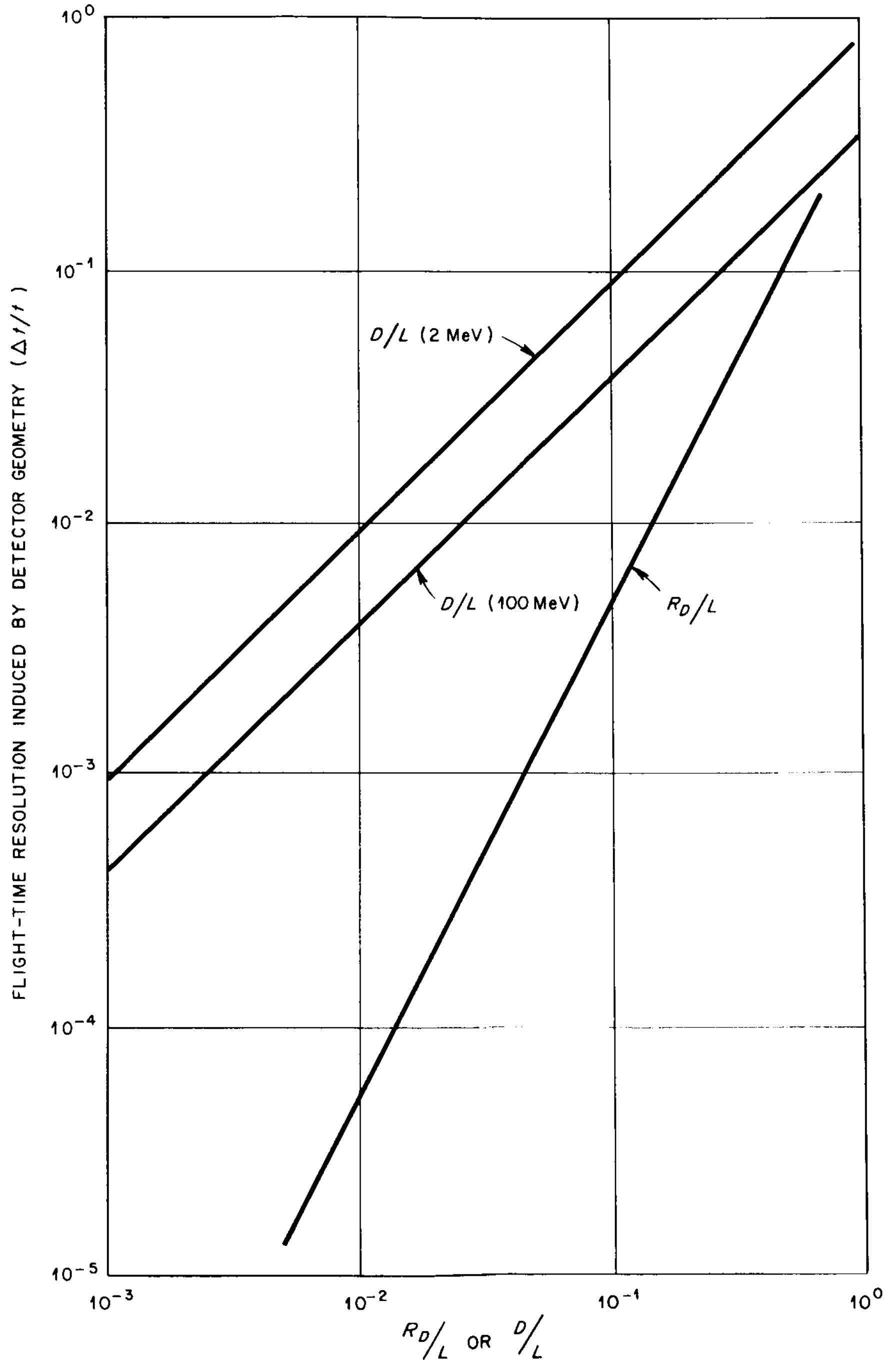

Figure 4. Flight-time resolution induced by detector geometry ($\Delta t/t$) versus R_D/L and D/L.

where A_D is the area of the detector face. In this approximation η_D is directly proportional to the detector volume. The expression for the maximum resolving time of detector in which both R_D and D are considered is

$$\frac{\Delta t}{t} \cong \frac{D}{L}\left(1 - \frac{Kv_n}{c}\right) + \frac{1}{2}\frac{R_D^2}{L^2} \qquad \text{III-8}$$

which is correct to the second order in R_D/L and D/L. Setting $R_D^2 = VOL/\pi D$ and taking the derivative of III-8 with respect to D, we get the thickness for which ($\Delta t/t$) is a minimum, under the constraint of constant volume (given spectrometer efficiency), or

$$D = \sqrt{\frac{VOL}{2\pi L}\left(1 - \frac{Kv_n}{c}\right)^{-1}} \quad . \qquad \text{III-9}$$

It follows from III-9 that for minimum $\Delta t/t$, R_D and D are related by

$$R_D^2 = 2DL\left(1 - \frac{Kv_n}{c}\right) \quad . \qquad \text{III-10}$$

Equation III-10 is the relationship for which the radial and axial dimension contribute equally to $\Delta t/t$. Equations III-7 through III-9 yield the smallest maximum flight-time resolution as a function of the spectrometer efficiency to be

$$\frac{\Delta t}{t} = \sqrt{\frac{2\eta_D}{\pi L \Sigma(v_n)}\left(1 - \frac{Kv_n}{c}\right)} \quad . \qquad \text{III-11}$$

It should be noted, however, that the relative dimensions specified by these equations will lead to poor angular resolution and/or inefficient light collection as one increases η_D. In practical applications R_D is therefore smaller than the value suggested by Equation III-10, so the thickness generally introduces the significant detector contribution to the geometric time resolution.

II. TARGET EFFECTS

The determination of the maximum flight-time resolution arising from the target dimensions requires a more detailed analysis. The flight-time uncertainties are a function of the rotation angles of the target and detector and the proton transit time through the target.

Inset C of Figure 3 shows the thick target geometry. The protons are incident on the target along the x-axis in a line beam. The target thickness along the beam axis is $S = T \sec\Psi$ where Ψ is the rotation angle of the target and T is the target thickness. The extreme flight-times which arise for a given target-detector configuration depend on the particle velocity ratio v_n/v_p and the detector rotation angle θ. For forward scattering angles and $v_n << v_p$, the longest and shortest flight-times are obtained at the target edges as shown in the figure. However, at given detector angles and increased neutron velocity, the maximum and minimum flight-times may reverse because the proton transit time through the target now comprises a significant fraction of the total flight time along a given path. In all cases when $\theta > 90^\circ$, corresponding to backward scattering, the maximum flight time is the sum of the proton transit time through the target and the neutron flight time along the longest path from the target to the detector; this value is always greater than the neutron flight time along the shortest path to the detector measured from the target edge.

Tha maximum and minimum flight times measured from the target edges are given with the aid of the cosine law as

$$t_2 = \frac{1}{v_n} (L^2 + S^2/4 + SL \cos\theta)^{1/2} - \frac{S}{2v_p} \qquad \text{III-12}$$

and

$$t_1 = \frac{1}{v_n} (L^2 + S^2/4 - SL \cos\theta)^{1/2} + \frac{S}{2v_p} \ , \qquad \text{III-13}$$

where θ is the detector rotation angle. S/v_p is the proton transit time through the target when v_p is the proton velocity. Expanding the square-root terms in III-12 and III-13 and following procedures outlined above, we obtain the result that

$$(\Delta t/t)_S \cong \left|\frac{S}{L} (\cos\theta - v_n/v_p)\right| \ . \qquad \text{III-14}$$

Equation III-14 is accurate through second order in S/L.

Depending on the detector rotation angle and the particle velocity ratio, given target-detector configurations arise where the maximum and minimum flight times given by Equations III-12 and III-13 are nearly equal For these cases, the minimum flight time occurs for interaction points within the target rather than at either target edge. Then, the total flight time is given by

$$t(x) = \frac{x}{v_p} + \frac{1}{v_n} (L^2 + x^2 - 2xL \cos\theta)^{1/2} \qquad \text{III-15}$$

where t(x) is the flight time measured from any point on x. Taking the derivative of III-15 with respect to x and solving for x/L when dt(x)/dx = 0, one obtains

$$\left(\frac{x}{L}\right)_{t=min} = -\frac{v_n}{(v_p^2 - v_n^2)^{1/2}} \sin\theta + \cos\theta \; ; \qquad \text{III-16}$$

the value of (x/L) for which t(x) is a minimum provided $v_p \neq v_n$. When $v_n = v_p$, there is a minimum at $\theta = 0$ independent of x.

Figure 5 shows the curves of $(x/L)_{t=min}$ versus θ for 2- and 100-MeV. neutrons. These data give the range of values of θ for which Equation III-14 is an invalid approximation for $(\Delta t/t)$. For the range 77°-88°, there is a minimum within the target when S/L = 0.1. Over this range of angles where $t(x) < \min(t_1, t_2)$ Equation III-14 should not be used. The minimum flight time is then determined from Equation III-15 using the values of $(x/L)_{t=min}$ and θ obtained from Figure 5 or Equation III-16. The

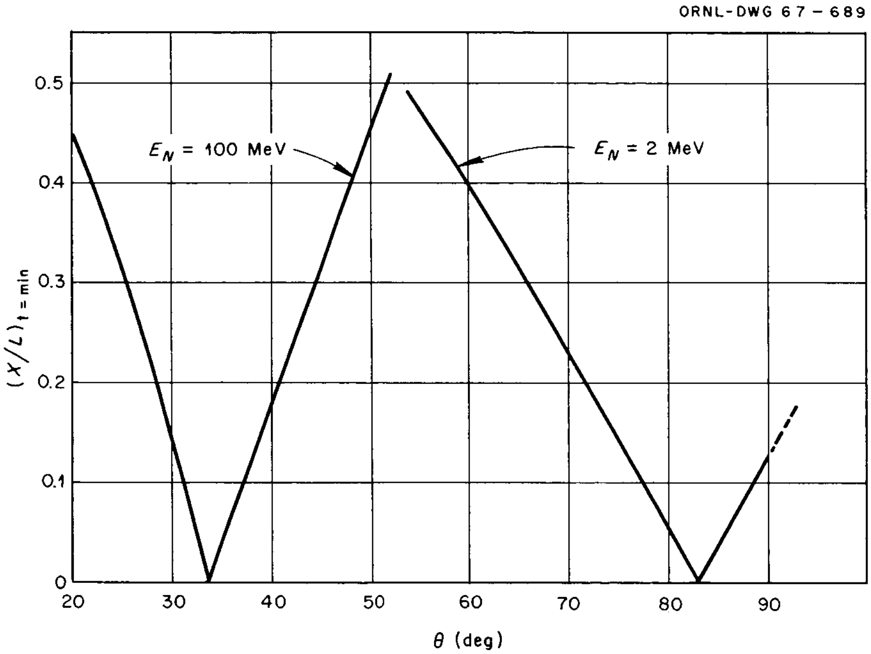

Figure 5. $(x/L)_{t\text{-min}}$ versus θ for 2- and 100-MeV. neutrons.

relative resolution time ($\Delta t/t$) is then calculated using the relation $[\max(t_1, t_2) - t(x)]/t$. For the case at θ given by $(x/L)_{t=\min} = 0$, the flight-time resolution is simply

$$\left(\frac{\Delta t}{t}\right)_S \cong \frac{S}{2L}\left(\cos\theta - \frac{v_n}{v_p}\right) + \frac{1}{8}\frac{S^2}{L^2} \quad . \qquad \text{III-17}$$

Figure 6 shows the geometric induced flight-time resolution plotted as a function of θ for $S/L = 0.1$ and 0.2 for 2- and 100-MeV. neutrons. The solid portion of each curve was obtained using Equation III-14. The dotted portion was obtained using Equation III-15; the range of angles being determined from Equation III-16 and Figure 5 for x/L just equal to the value at the target edges.

The calculation of the effects on the flight-time resolution arising from the target radius follows similar arguments. Inset D of Figure 3 shows the thin target configuration in which the radial dimension introduces the dominant flight-path uncertainty. In this case, the proton beam is taken as uniformly distributed over the target radius.

Ignoring multiple scattering of the protons in the target, the "effective" target radius corresponds to the radial dimension of the beam, which in most applications is smaller than the target radius. If the cartesian components of the beam are studied separately, we observe that the z-component of the beam produces a ΔL which is independent of the detector rotation angle, θ. The calculation of the maximum timing uncertainties from the z-component yields a solution similar to

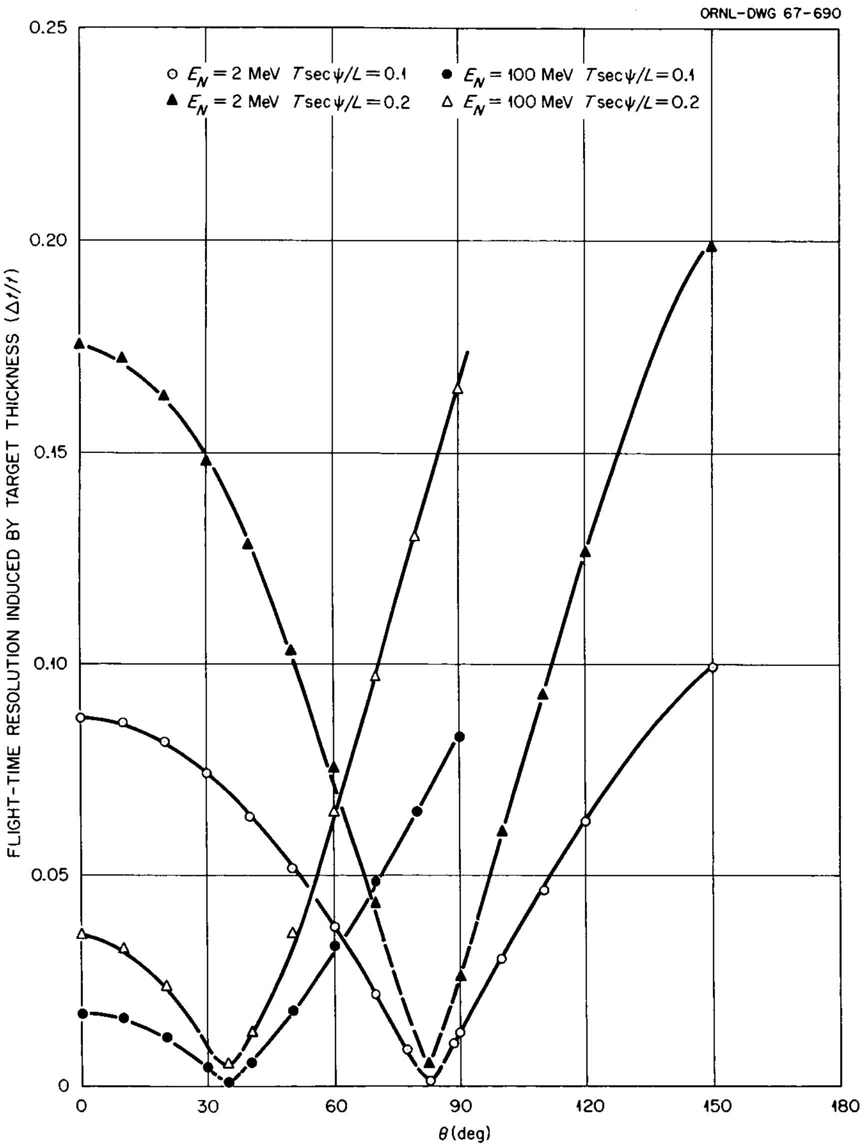

Figure 6. Flight-time resolution induced by target thickness $(\Delta t/t)_S$ versus θ for 2- and 100-MeV. neutrons for the cases where T sec Ψ/L = 0.1 and 0.2.

Equation III-4 obtained for the detector radius. The uncertainties are of second order in R_T/L. The y-component of the beam, on the other hand, produces a ΔL which is dependent on θ and Ψ and contains first order terms in R_T/L. On the generally valid assumption that the beam radius is smaller than the detector radius, the maximum flight-time uncertainties can be calculated in the x-y plane with no practical loss in generality. For those cases where the beam radius is comparable to the detector radius, the contribution from the z-component can be added in quadrature with that obtained for the y-component.

When the maximum and minimum flight times occur at the target edges, we obtain the expressions for the extremum flight times from the cosine law as

$$t_2 = \frac{1}{v_n}\,[L^2 + R_T^2 - 2R_TL\,\sin(\theta - \Psi)]^{1/2} - \frac{R_T\,\sin\Psi}{v_p} \qquad \text{III-18}$$

and

$$t_1 = \frac{1}{v_n}\,[L^2 + R_T^2 + 2R_TL\,\sin(\theta - \Psi)]^{1/2} + \frac{R_T\,\sin\Psi}{v_p} \qquad \text{III-19}$$

where R_T is the target radius. Expanding the square-root terms and dividing the difference $|t_2 - t_1|$ by the nominal flight time t yields

$$\left(\frac{\Delta t}{t}\right)_{R_T} \cong \left|\frac{2R_T}{L}\left[\sin(\theta - \Psi) + \frac{v_n}{v_p}\,\sin\Psi\right]\right| \qquad \text{III-20}$$

which is accurate through second order in R_T/L. Equation III-20 is an approximation to the flight-time resolution which may be used provided the target edges yield the maximum and minimum flight times. For the other case, the actual minimum flight time exists for a point within the target.

For neutrons born at a point η in the target, the flight time is given by

$$t(\eta) = \frac{1}{v_n} [L^2 + \eta^2 - 2\eta L \sin(\theta - \Psi)]^{1/2} - \frac{\eta \sin\Psi}{v_p} . \qquad \text{III-21}$$

Taking the derivative of III-21 with respect to η and solving for (η/L) when $[dt(\eta)/d\eta] = 0$, we obtain the value of $(\eta/L)_{t=min}$ for which $t(\eta)$ is a minimum. The result is

$$\left(\frac{\eta}{L}\right)_{t=min} = -\frac{v_n \sin\Psi \cos(\theta - \Psi)}{(v_p^2 - \sin^2\Psi\ v_n^2)^{1/2}} + \sin(\theta - \Psi) . \qquad \text{III-22}$$

The equations which describe the target radius dependent time resolution are a function of the rotation angles θ and Ψ as well as the particle velocity ratio. A typical case is discussed here. Figure 7 shows the results of plotting $(\eta/L)_{t=min}$ as a function of θ for 2-MeV. neutrons. The target is rotated at 30° to the incident beam. Assuming $R_T/L = 0.1$, we observe from Figure 7 that for the range of angles from 28° to 39°, the minimum is within the target and Equation III-20 should

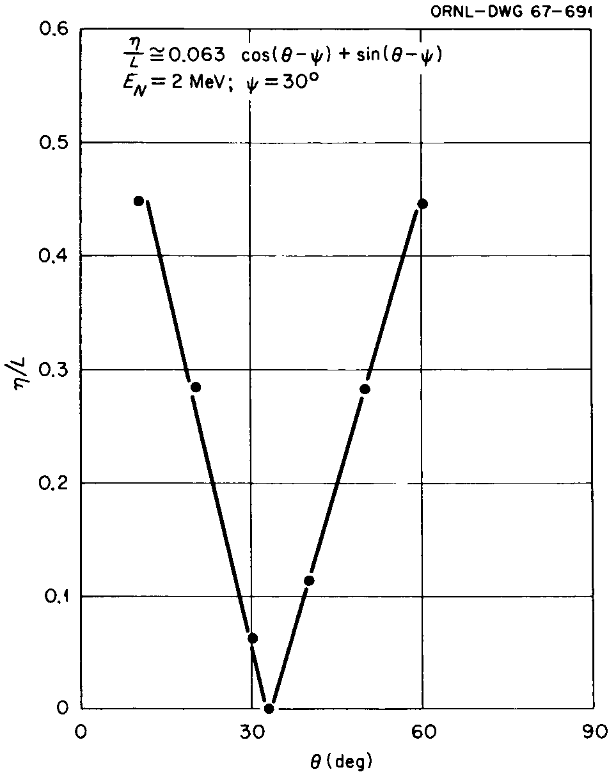

Figure 7. (η/L) versus θ for 2-MeV. neutrons and Ψ - 30° for the special case where $(\eta/L) \cong 0.063 \cos(\theta - \Psi) + \sin(\theta + \Psi)$.

not be used to evaluate $\Delta t/t$. Instead the minimum flight time is evaluated using Equation III-21 when $t(\eta) < \min(t_1, t_2)$ using the values of η/L and θ from Figure 7 for the given target rotation angle Ψ. If $t(\eta) \leq \min(t_1, t_2)$ Equation III-21 is used to compute $\Delta t/t$ where $\Delta t/t = [\max(t_1, t_2) - t(\eta)]/t$. For the case at θ when $(\eta/L)_{t=\min} = 0$, the relative timing uncertainty is given by

$$\left(\frac{\Delta t}{t}\right)_{R_T} \doteq \frac{R_T}{L}\left[\sin(\theta - \Psi) - \frac{v_n}{v_p}\sin\Psi\right] + \frac{1}{2}\left(\frac{R_T}{L}\right)^2 + \dots \quad . \qquad \text{III-23}$$

The results of these calculations are illustrated in Figure 8. The solid portion of the curve is obtained from Equation III-20 and the dashed portion using Equation III-21; the values for θ and η/L being determined from Figure 7.

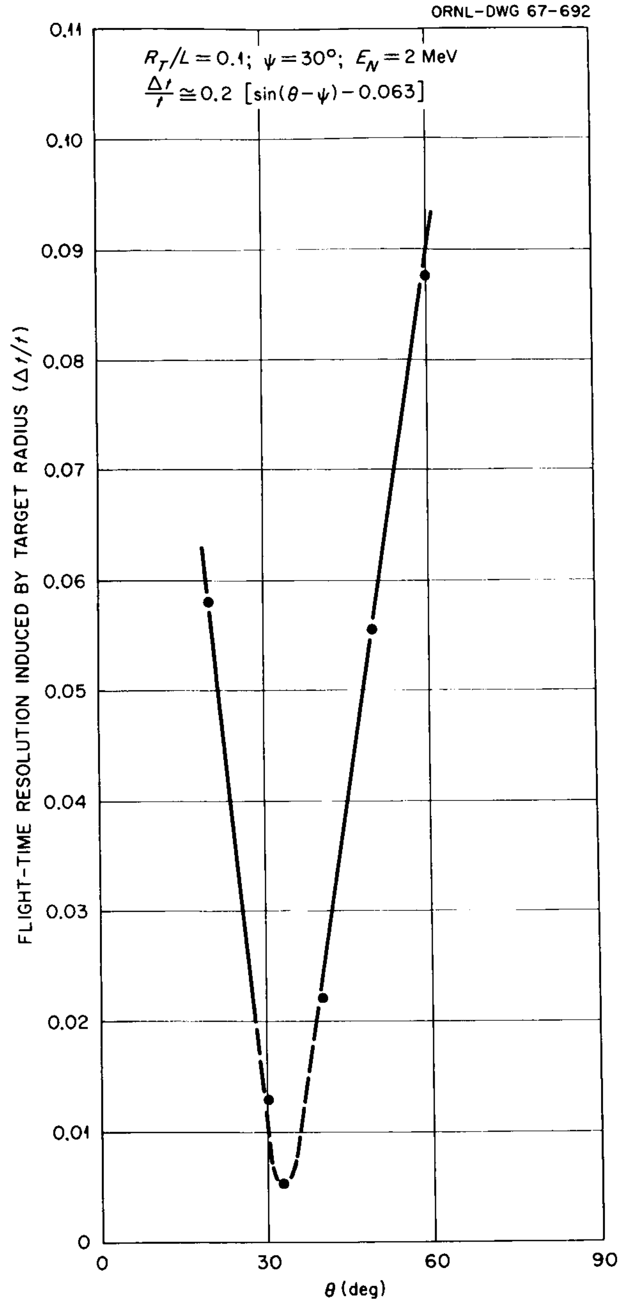

Figure 8. Flight-time resolution induced by target radius $(\Delta t/t)_{R_T}$ versus θ for the case where $R_T/L = 0.1$, $\Psi = 30°$ and $E_N = 2$ MeV.

CHAPTER IV

THE TIME CHANNEL RESPONSE FUNCTION

The simplified spectrometer defined in Chapter I is analyzed in terms of the time-channel response function $S_k(v_p;v_n,\theta)$; the probability per MeV. of neutron energy per incident proton that a neutron of speed v_n produced in the target is detected in channel k of the multichannel-time analyzer. The time-channel response function is derived from the convolution of the flight-time distribution function and the time slewing response function and the integral over the analyzer sensitivity function. Each of these functions will be discussed in detail.

S_k includes the "response" of the target through its differential neutron production cross section $\Sigma_p(v_p;v_n,\theta)$. The sum of S_k over all time channels is related to the counter efficiency by

$$\sum_k S_k(v_p;v_n,\theta) \cong \epsilon_D(v_n)\,\frac{A_D}{L^2}\,\Sigma_p(v_p;v_n,\theta)S_{eff} \qquad \text{IV-1}$$

where S_{eff} is the target thickness along the beam direction taking into account the beam attenuation.

I. THE PHYSICAL FLIGHT-TIME DISTRIBUTION OF DETECTED NEUTRONS AVERAGED OVER THE TARGET

The flight-time distribution G is calculated here for neutrons which are born in the target and interact in the detector in terms of the physical flight time of Equation II-5. The distribution function is obtained by defining the geometric response function for neutron interaction events in the detector as a function of the neutron flight time from a point in the target and then summing over the target volume. The flight-time density function of detected neutrons is the probability per incident proton of speed v_p per MeV. of neutron energy per nsec. that a secondary neutron of speed v_n has an apparent flight time t, and is given by

$$G(v_p;v_n,t)\,dt = dt \iiint N(y,z)\,B(\ell_p,\vec{\Omega})\,E_\theta(t,\ell_p,x,v_n)\,dxdydz \qquad \text{IV-2}$$

where dxdydz is an element of target volume and

$N(y,z)\,dydz$ = the probability that a beam particle has a displacement from the beam axis within dy at y and dz at z,

$B(\ell_p,\vec{\Omega})\,dx$ = the probability per unit solid angle per MeV. of neutron energy that the proton interacts in the target within dx at a penetration $\ell_p = x + y \times \tan\Psi - \tau_1 \sec\Psi$ to produce a neutron which is emitted in the direction $\vec{\Omega}$, and

$E_\theta(t,\ell_p,x,v_n)\,dt$ = the detector geometric response function: The probability that a neutron of velocity v_n born at x,y in the target and emitted in a unit solid angle toward the detector is detected within dt at t.

The Detector Geometric Response Function

The detector geometric response function is given by

$$E_\theta(t,\ell_p,x,v_n)\,dt = dt \int_{A_D} I(t,\ell_p,x,v_n,\vec{\Omega})\,d\vec{\Omega} \qquad \text{IV-3}$$

where the integration is performed over the area of the detector face, A_D. We assume for all cases that the y' and z' dimension of the detector front surface are greater than those of the beam intersection on the target. $d\vec{\Omega} = [(\hat{i}' \cdot \hat{\Omega})/\ell_f^3]dA_D$ is the element of solid angle subtended by an element of detector front surface at the interaction point in the target $P_T(x,y,z)$. ℓ_f is the distance from P_T to face of the detector and $\hat{i}'$ is the unit vector along the detector axis x'. The integrand, the probability that a neutron of velocity v_n born in the target at x,y and emitted in the direction $\vec{\Omega}$ is detected within dt at t, is given by

$$I(t,\ell_p,x,v_n,\vec{\Omega})\ dt$$

$$= \begin{cases} \exp\left(-\Sigma_{TN}^{eff}\ \ell_T\right)\Sigma(v_n)\ \exp\left[-\Sigma_D^{eff}\ \ell_D(t)\right]\ d\ell_D(t)\ ; & \text{provided the neutron interacts at a detector penetration distance } \ell_D(t) \text{ along the direction } \vec{\Omega} \\ 0\ ; & \text{for } \ell_D(t) \text{ inconsistent with neutron interactions in the detector} \end{cases} \qquad \text{IV-4}$$

where

Σ_{TN}^{eff} = effective macroscopic absorption cross section for neutrons in the target,

$\Sigma(v_n)$ = macroscopic "efficiency" cross section for neutron detection,

Σ_D^{eff} = effective macroscopic absorption cross section for neutrons in the detector,

v_n = neutron velocity,

ℓ_T = pathlength traveled by the neutron in the target,

$\ell_D(t)$ = pathlength traveled by the neutron in the detector expressed in terms of the apparent flight time,

$d\ell_D(t)$ = differential distance traveled by the neutron in time dt.

The shape of $I(t,\ell_p,x,v_n,\vec{\Omega})$ in time is just an exponential truncated at the time limits corresponding to the time at which the neutron would pass through the front and rear surfaces of the detector. The combination of these exponentially shaped distributions for various points on the detector surface complicates the original simple shape.

Once ℓ_D has been written as an explicit function of t, Equation IV-3 gives the distribution of neutron flight times summed over the detector volume; the volume element in the detector having been defined in terms of dA_D and $v_n dt$.

The distance traveled by the neutron from its birth point in the target $P_T(x,y,z)$ to the point of detection P_D is $t_n v_n$. With the aid of Equation II-5 with $t_j = t_w(h) = 0$, we can write

$$t_n v_n = \ell_f + \ell_D(t) = (t - t_c - t_p)v_n \qquad \text{IV-5}$$

where ℓ_f is the distance traveled by the neutron from P_T to a point on the face of the detector and $\ell_D(t)$ is the distance from the detector face to the point of detection P_D. It has been assumed that the light from the neutron interactions is normally incident on the photocathode. Then the light transit time from the point of neutron interaction to the photocathode is

$$t_c = \frac{K}{c}\,[D - \ell_D(\hat{i}' \cdot \hat{\Omega})] \quad , \qquad \text{IV-6}$$

where $(\hat{i}' \cdot \hat{\Omega})$ is the angle at which the neutron strikes the face of the detector. Substituting Equation IV-6 into Equation IV-5 and solving for ℓ_D, yields the result

$$\ell_D(t) = \frac{[t - t_p - (KD/c)]v_n - \ell_f}{\Delta} , \qquad \text{IV-7}$$

and

$$d\ell_D(t) = \frac{v_n \, dt}{\Delta} , \qquad \text{IV-7A}$$

where $\Delta = [1 - (Kv_n/c)(\hat{i}' \cdot \hat{\Omega})]$. As the denominator goes to zero, the only problems introduced are numerical and I is nonzero only over a small time band.

The proton transit time through the target, t_p, is obtained assuming the time reference is at $x = 0$ with the target imagined to be absent. Then if dE/dx is considered constant through the target,

$$t_p \cong \frac{x}{v_p} + \frac{\ell_p^2}{4E_p v_p} \left(-\frac{dE}{dx}\right) , \qquad \text{IV-8}$$

where E_p is the proton energy (MeV.) and $-(dE/dx)$ is the incremental energy loss for protons in the target material. $-(dE/dx)$ is a positive number. The derivation of t_p is given in Appendix A, while Appendix B contains the detailed analysis leading to expressions for $(\hat{i}' \cdot \hat{\Omega})$, ℓ_f, and ℓ_T.

Integrals Over the Target Volume

To obtain the complete flight-time distribution given by Equation IV-2, we must now integrate over the target volume taking into consideration all possibilities for proton interactions. In that equation,

$$B(\ell_p,\vec{\Omega})\,dx = \begin{cases} \Sigma_p(v_p;v_n,\vec{\Omega}) \exp\left(-\Sigma_{TP}^{eff}\,\ell_p\right) dx\ ; & x,\ y \text{ within target} \\ 0 & x,\ y \text{ outside target} \end{cases} \qquad \text{IV-9}$$

where

$\Sigma_p(v_p;v_n,\vec{\Omega})$ = the differential cross-section per MeV. per unit solid angle in the direction $\vec{\Omega}$ for the production of neutrons of speed v_n,

Σ_{TP}^{eff} = the effective cross section for absorption of protons in the target.

Since the chance of emission of the neutron is taken to be independent of the azimuthal angle, $\Sigma_p(v_p;v_n,\vec{\Omega})$ reduces to $\Sigma_p(v_p;v_n,\Theta)$, where Θ is the angle of neutron emission relative to the beam axis. If $\Sigma_p(v_p;v_n,\Theta)$ does not vary too rapidly with Θ or v_p, it may also be considered constant in the integral for G. [Experiments are normally designed to make $\Sigma_p(v_p;v_n,\Theta)$ sufficiently constant over the detector face so that $\Sigma_p(\Theta) \cong \Sigma_p(\theta)$].

It has been shown in Chapter III that the z-component of the beam typically introduces negligible flight-path variations. Based on these results, $E_\theta(t,\ell_p,x,v_n)$ and $B(\ell_p,\vec{\Omega})$ were considered independent of z, and since N(y,z) is the only term in which z is contained explicitly, it is integrated immediately over all values of z with the result that

$$dy \int N(y,z)\, dz = N(y)\, dy \quad . \qquad \text{IV-10}$$

N(y) is approximated by a gaussian distribution with mean value equal to zero, given by

$$N(y) = \frac{1}{\sigma\sqrt{2\pi}}\, e^{(-1/2)(y/\sigma)^2} \qquad \text{IV-11}$$

where

σ = the standard deviation of the proton beam distribution about the x-z plane.

II. THE EFFECTS OF INSTRUMENTAL TIME JITTER

There is a spread in the duration of the time intervals between the production of photoelectrons resulting from the neutron interaction in the detector and the time when the amplitude of the output pulse triggers the electronic circuitry. This time spread depends on several factors including the energy left behind by the particle in the scintillator, the conversion efficiency of the scintillator, and the statistical variations in the cathode photoelectron emission and in the electron multiplier tube. The magnitude of the timing jitter depends on the fluctuations in all of these causes as well as the amplitude of the pulses introduced by the light output in the detection event. The amplitude variations are treated in Section IV of this chapter and the time jitter is handled separately under the assumption that it is independent of amplitude variations in the output pulse.

Included in the jitter distribution are the fluctuations arising from the distribution of the protons in time and the time variations introduced by the zero-time detector. These uncertainties, along with those described above, are here lumped into one constant source of instrumental time jitter.

The jitter manifests itself in a broadening of the apparent flight-time distribution. The causes of jitter arise randomly in time so that the time-jitter distribution can be approximated by a normal frequency function with zero mean jitter time and constant standard deviation σ_j, given by

$$J(t_j) = \frac{1}{\sigma_j\sqrt{2\pi}} e^{(-1/2)(t_j/\sigma_j)^2} \quad . \qquad \text{IV-12}$$

The jitter-smeared apparent flight time t_i for an event is

$$t_i = t + t_j \quad . \qquad \text{IV-13}$$

Then, the jitter-smeared flight-time distribution function is obtained by the convolution of Equation IV-12 with IV-2:

$$dt_i \; C(v_p;v_n,t_i) = dt_i \int G(v_p;v_n,t) \; J(t_i - t) \; dt \quad . \qquad \text{IV-14}$$

Completing the integration of Equation IV-14 proceeds as follows. Equation IV-7 is inserted into Equation IV-4 and all terms containing the physical flight time t are factored out. These terms, along with Equation IV-12, are placed inside the integral sign in Equation IV-14. Completing the square of the terms in t and integrating over all values of t yields the following result

$$dt_i \; C(v_p;v_n,t_i) = dt_i \; v_n\Sigma(v_n) \; \Sigma_p(v_p;v_n,\theta) \iiint N(y) \; B(\ell_p,\vec{\Omega})\left(e^{-\Sigma_{TN}^{eff} \ell_T/\Delta}\right)$$

$$\times \; \exp\left[\left(\Sigma_D^{eff}/\Delta\right)(\ell_f + KDv_n/c + t_p v_n)\right] \qquad \text{IV-15}$$

$$\times \exp\left[-\frac{1}{2\sigma_j^2}(t_i^2 - \Xi^2)\right] \left[\operatorname{erf}\left(\frac{t_{max} - \Xi}{\sigma_j}\right) - \operatorname{erf}\left(\frac{t_{min} - \Xi}{\sigma_j}\right)\right] d\vec{\Omega}dxdy \quad ,$$

where

$$\Delta = 1 - (Kv_n/c)(\hat{i}' \cdot \hat{\Omega}) \qquad \text{IV-15A}$$

and

$$\Xi = t_i - \sigma_j^2 \; \Sigma_D^{eff} \; v_n/\Delta \quad . \qquad \text{IV-15B}$$

t_{min} and t_{max} are the minimum and maximum physical flight times t along the direction $\vec{\Omega}$ to the front surface and point of exit of the detector. t_{min} and t_{max} are given by

$$t_{min} = t_p + \ell_f/v_n + KD/c$$

and

$$t_{max} = t_p + \ell_f/v_n + (D/v_n)/(\hat{i}' \cdot \hat{\Omega}) \qquad \text{IV-17}$$

from Equations IV-5 through IV-7. The error function used here is defined by

$$\frac{1}{a\sqrt{2\pi}} \int_{\ell_1}^{\ell_2} e^{-x^2/2a^2}\, dx = \text{erf}\, \frac{\ell_2}{a} - \text{erf}\, \frac{\ell_1}{a} \qquad \text{IV-18}$$

In practical calculations, the quantity $C(v_p;v_n,t_i)/\Sigma_p(v_p;v_n,\theta)$ is evaluated since the purpose is to calculate $\Sigma_p(v_p;v_n,\theta)$ from experimental results.

III. RELATIONS LEADING TO THE DETECTOR EFFICIENCY

The integral of Equation IV-14 over the jitter-smeared flight time t_i should yield the efficiency of the detector ϵ_D times the number $\mathcal{F}$ of neutrons which strike the face of the detector, or

$$\int_{t_i} dt_i \int_t dt\; G(v_p;v_n,t)\; J(t_i - t) \overset{?}{=} \epsilon_D \mathcal{F} \qquad \text{IV-19}$$

where

$$\mathcal{F} = \Sigma_p(v_p;v_n,\theta)\; T_{eff} \int_{A_D} d\vec{\Omega} \quad .$$

T_{eff} is the effective target thickness given by

$$T_{eff} = \left(1/\Sigma_{TP}^{eff}\right) \left[1 - e^{-\Sigma_{TP}^{eff} S}\right] , \qquad \text{IV-20}$$

if the neutron attenuation in the target is ignored. In this section, we shall perform the integration indicated in Equation IV-19 in order to prove the validity of the relationship.

Changing the order of integration in Equation IV-19 and performing the inner integration yields the result

$$\int_t G(v_p;v_n,t)\, dt \overset{?}{=} \epsilon_D \mathcal{F} \quad . \qquad \text{IV-21}$$

It is possible to perform the integration in this manner since $J(t_j)$ is normalized to unity. The convolution of any function with one of unit area yields a function with the same area as that under the original function.

In the assumption that no neutron attenuation occurs in the target, Equation IV-4 reduces to

$$dt\ I'(t,\ell_p,x,v_n,\vec{\Omega}) = \Sigma(v_n) \exp[-\Sigma_D \ell_D(t)]\ d\ell_D(t) \quad . \qquad \text{IV-22}$$

Since this is the only equation in which t is contained explicitly, it may be integrated over t immediately. Substituting $\ell_D(t)$ and $d\ell_D(t)$ from Equations IV-7 and IV-7A into IV-22 and integrating from t_{min} to t_{max}

We obtain the result that

$$\int_{t_{\min}}^{t_{\max}} I'(t,\ell_p,x,v_n,\vec{\Omega})\,dt$$

$$= \frac{\Sigma(v_n)}{\Sigma_D}\left[1 - \exp\left(-\Sigma_D \frac{D}{\hat{i}' \cdot \hat{\Omega}}\right)\right] \equiv \epsilon_D(\ell_p,x,v_n,\vec{\Omega}) \qquad \text{IV-23}$$

where $t_{\min}$ and $t_{\max}$ are given by Equations IV-16 and IV-17, respectively, and $D/(\hat{i}' \cdot \hat{\Omega})$ is the distance traveled along the direction $\vec{\Omega}$ by the neutron in passage through the detector.

Now, with the aid of Equation IV-2, we can write

$$\epsilon_D\mathcal{F} = \int_y \int_{x(y)} \int_{A_D} \epsilon_D(\ell_p,x,v_n,\vec{\Omega})\, N(y)\, B(\ell_p,\vec{\Omega})\, d\vec{\Omega}dxdy \quad . \qquad \text{IV-24}$$

$\epsilon_D(\ell_p,x,v_n,\vec{\Omega})$ is a function of the coordinates of the neutron birth point in the target and the direction of emission of the neutron. If the direction of emission of the neutron is such that it passes through the detector front surface, then Equation IV-4 is nonzero. Further, the spectrometer efficiency, given by the product of the detector efficiency ϵ_D and the element of solid angle subtended by the detector, does not depend strongly on the neutron birth coordinates. Then Equation IV-24 may be integrated as follows

$$\left\langle \int_{A_D} \epsilon_D(v_n,\vec{\Omega})d\vec{\Omega} \right\rangle_{\text{target}}$$

$$= \frac{\int_y \int_{x(y)} \int_{A_D} \epsilon_D(\ell_p,x,v_n,\vec{\Omega})\ N(y)\ B(\ell_p,\vec{\Omega})\ d\vec{\Omega}dxdy}{\int_y \int_{x(y)} N(y)\ B(\ell_p,\vec{\Omega})\ dx\ dy} \qquad \text{IV-25}$$

where $\left\langle \int \epsilon_D(v_n,\vec{\Omega})\ d\vec{\Omega} \right\rangle_{\text{target}}$ is the average spectrometer efficiency weighted by the interaction density in the target. In this analysis, ϵ_D is considered essentially constant over the detector area, so that

$$\overline{\epsilon_D(v_n)} = \frac{\left\langle \int_{A_D} \epsilon_D(v_n,\vec{\Omega})\ d\vec{\Omega} \right\rangle_{\text{target}}}{\Delta\Omega_o} \quad . \qquad \text{IV-26}$$

$\overline{\epsilon_D(v_n)}$ is just the average value of the detector efficiency and $\Delta\Omega_o = \int_{A_D} d\vec{\Omega}$ is the element of solid angle measured relative to the origin of the target coordinate system. Now, we can write

$$\overline{\epsilon_D(v_n)}\ \Delta\Omega_o \int_y \int_{x(y)} N(y)\ B(\ell_p,\theta)\ dxdy \overset{?}{=} \epsilon_D\mathcal{F} \qquad \text{IV-27}$$

since $\Sigma_p(v_p;v_n,\vec{\Omega}) \rightarrow \Sigma_p(v_p;v_n,\theta)$. The integration in Equation IV-24 has now been greatly simplified.

The limits of integration for the x and y integrals are given by

$$\tau_1 \sec\Psi - y \tan\Psi \le x \le \tau_2 \sec\Psi - y \tan\Psi \qquad \text{IV-28}$$

and

$$-2.5\sigma \le y \le 2.5\sigma \qquad \text{IV-29}$$

Introducing IV-9 and IV-11 into IV-27 and completing the integration over the specified limits, we obtain

$$\overline{\epsilon(v_n)}\, \Sigma_p(v_p;v_n,\theta) \left(1/\Sigma_{TP}^{eff}\right) \left(1 - e^{-\Sigma_{TP}^{eff} S}\right) \Delta\Omega_0 = \epsilon_D \mathcal{F} \quad . \qquad \text{IV-30}$$

Then, the integral of Equation IV-19 over the physical flight time yields the average value of the detector efficiency weighted over the target.

IV. THE TIME-SLEWING RESPONSE FUNCTIONS

The large amplitude range in the light output from the neutron interaction causes a portion of the pulse amplitude spread to be translated into a timing spread which is called slewing or walk. The time-slewing response function $W[t_w(h),v_n]\, dt_w(h)$ is defined as the probability that a neutron of velocity v_n produces an amplitude-dependent slewing time within $dt_w(h)$ at $t_w(h)$. The response function is normalized such that the integral over all values of $t_w(h)$ is unity,

$$\int_{t_w(h)} W[t_w(h),v_n]\, dt_w(h) = 1 \quad . \qquad \text{IV-31}$$

In order to determine the slewing response function, the pulse-height spectrum resulting from the neutron interactions in the detector and the time-slewing curve must be known. The pulse-height spectrum is calculated using a first collision approximation to obtain the differential macroscopic cross section. Conversion of these data to the corresponding pulse-height spectrum is accomplished using the fast-light output curves for charged-particle interactions in the detector. The slewing curve which gives the time shift in terms of the ratio of the pulse height to the amplitude of the output pulse which just triggers the time analyzer, was taken directly from the data of Peelle *et al.*[24]

Derivation of the Pulse-Height Spectrum

Neutron detection is achieved in organic scintillators by the elastic scattering on hydrogen nuclei and the nonelastic interactions with carbon nuclei. Both give energetic charged particles which produce light in the scintillator.

The cross sections for these reactions will be derived using the method and notation of Schuttler,[25] and the resulting energy spectra converted to pulse-height spectra in light-output units using the fast light-output curves of both Schuttler and Birks.[26]

---

[24] R. W. Peelle *et al.*, *Differential Cross Sections for the Production of Protons in the Reactions of 160-MeV. Protons on Complex Nuclei*, ORNL-3887, September 1966.

[25] R. S. Schuttler, *Efficiency of Organic Scintillators to Fast Neutrons*, ORNL-3888, July 1966.

[26] J. B. Birks, *Proc. Phys. Soc.* **A64**, 74 (1952).

In this analysis, we are assuming that the charged particles from the hydrogen reactions are totally absorbed in the scintillator. For example, for 2.54-cm. thick detectors, the assumption is valid for neutrons up to 14.5 MeV. where the maximum range of the charged particle is 0.23 cm. For 50-MeV. neutrons, however, the range of the charged particle is 2.20 cm. which is comparable with the detector thickness, and the resulting spectrum is in error.

Hydrogen scattering. In the energy region below 10 MeV., (n,p) scattering is isotropic in the center-of-mass system and all proton energies from E_N down to zero are equally possible after a single scattering. At neutron energies greater than 10 MeV., the scattering becomes increasingly anisotropic.

The energy differential macroscopic cross section for elastic scattering of a neutron of energy E_N in hydrogen is given by

$$\Sigma_H(E_N;E_p) = \pi\sigma(E_N;\theta)\ N_H(E_N \cos\theta)^{-1} \qquad \text{IV-32}$$

where $\sigma(E_N,\theta)$ is the laboratory microscopic differential cross section for scattering at angle θ and N_H is the atomic density of hydrogen in the scintillator. $\sigma(\theta)$ is approximated using semiempirical formulae due to Gammel.[27] The relationship between E_p and θ is obtained from classical kinematics as

---

[27] J. L. Gammel, Fast Neutron Physics, Part II, (Interscience Publishers, New York, 1963), p. 2209.

$$E_p = \frac{1}{2} E_N (1 - \cos 2\theta) = E_N \sin^2\theta \quad . \qquad \text{IV-33}$$

The energy differential cross section is obtained for values of θ in the range $0^\circ \leq \theta \leq 90^\circ$. Equation IV-33 yields the value of E_p which when replaced in IV-32 gives the value of $\Sigma_H(E_N, E_p)$.

Figure 9, taken directly from the work of Schuttler,[28] shows the proton-energy differential macroscopic cross section for elastic scattering on hydrogen plotted as a function of the proton energy for several values of the neutron energy.

Reactions in carbon. At neutron energies greater than 10 MeV., the probability for nonelastic scattering with carbon becomes important. The most important ground state reactions which compose the nonelastic cross sections and which give charged particles are

1. $C(n,n')C^*$ leading to $C^* \rightarrow 3\alpha$; $Q \geq -7.8$ MeV.,
2. $^{12}C(n,p)^{12}B$; $Q = -12.6$ MeV. and $^{12}C(n,np)^{11}B$; $Q = -18.4$ MeV.,
3. $^{12}C(n,\alpha)^9Be$; $Q = -5.7$ MeV.

The cross sections for the reactions described in 1 and 2 above have been calculated by Schuttler[29] using an adaptation of the Monte Carlo code of Bertini[30] which is based on the intranuclear cascade model. Schuttler's analysis did not produce ground state reactions (n,α) leading to ^9Be.

---

[28] Schuttler, op. cit., p. 21.

[29] Schuttler, op. cit., p. 28.

[30] H. Bertini, Phys. Rev. 131, 1801 (1963); also Monte Carlo Calculations on Intranuclear Cascades, ORNL-3383 (1963).

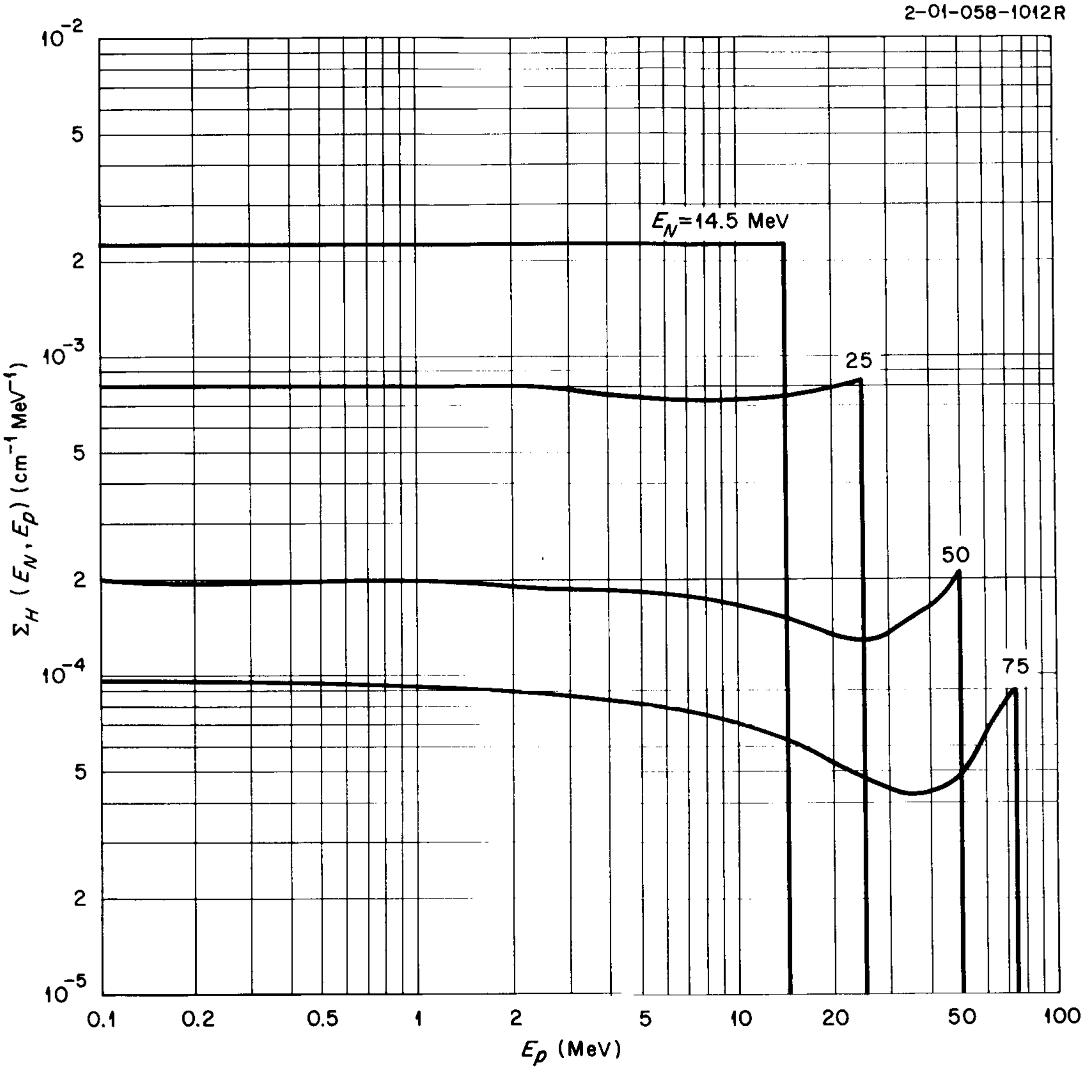

Figure 9. Proton energy differential macroscopic cross section for elastic scattering on hydrogen. The values of $\Sigma_H(E_N;E_p)$ were computed with the hyrodgen density in the scintillator taken as 0.0452×10^{24} atoms/cm.^{3}

We shall adopt his method for deriving the differential cross section for this reaction.

It is assumed that the reaction products from the (n,α) reaction are isotropic in the center-of-mass system. The differential macroscopic cross section for the production of alpha particles is then given by

$$\Sigma_{C(n,\alpha)}(E_N;E_\alpha) = \begin{cases} N_C\sigma_\alpha\,(E_{\alpha\max} - E_{\alpha\min})^{-1}; & E_{\alpha\min} \le E_\alpha \le E_{\alpha\max} \\ 0 & ;\ \text{otherwise} \end{cases} \qquad \text{IV-34}$$

where σ_α is the total cross section for this reaction, N_C is the atomic density of carbon in the scintillator, and $E_{\alpha\max}$ and $E_{\alpha\min}$ are the maximum and minimum possible α-particle energy values. $E_{\alpha\max}$ and $E_{\alpha\min}$ were calculated using the momentum relations assuming that only the neutron is relativistic. The cross section is then taken as being uniform in the corresponding energy region. This approximation is reasonable since $\sigma_\alpha \le 0.1\ \sigma_C$ (nonelastic) over the allowed energy region for which the reaction is possible and the contribution to the total pulse-height spectrum is small compared to the hydrogen and other carbon reactions.

Figure 10 shows the relative differential cross section for the cascade reaction plotted by Schuttler[31] as a function of the electronic bias (in light units) for a 2.54-cm. thick scintillator. The detailed analysis leading to this cross section is given in ref. 20. For the purpose of this analysis, we derive a standard energy spectrum based on

---

[31] Schuttler, op. cit., p. 36.

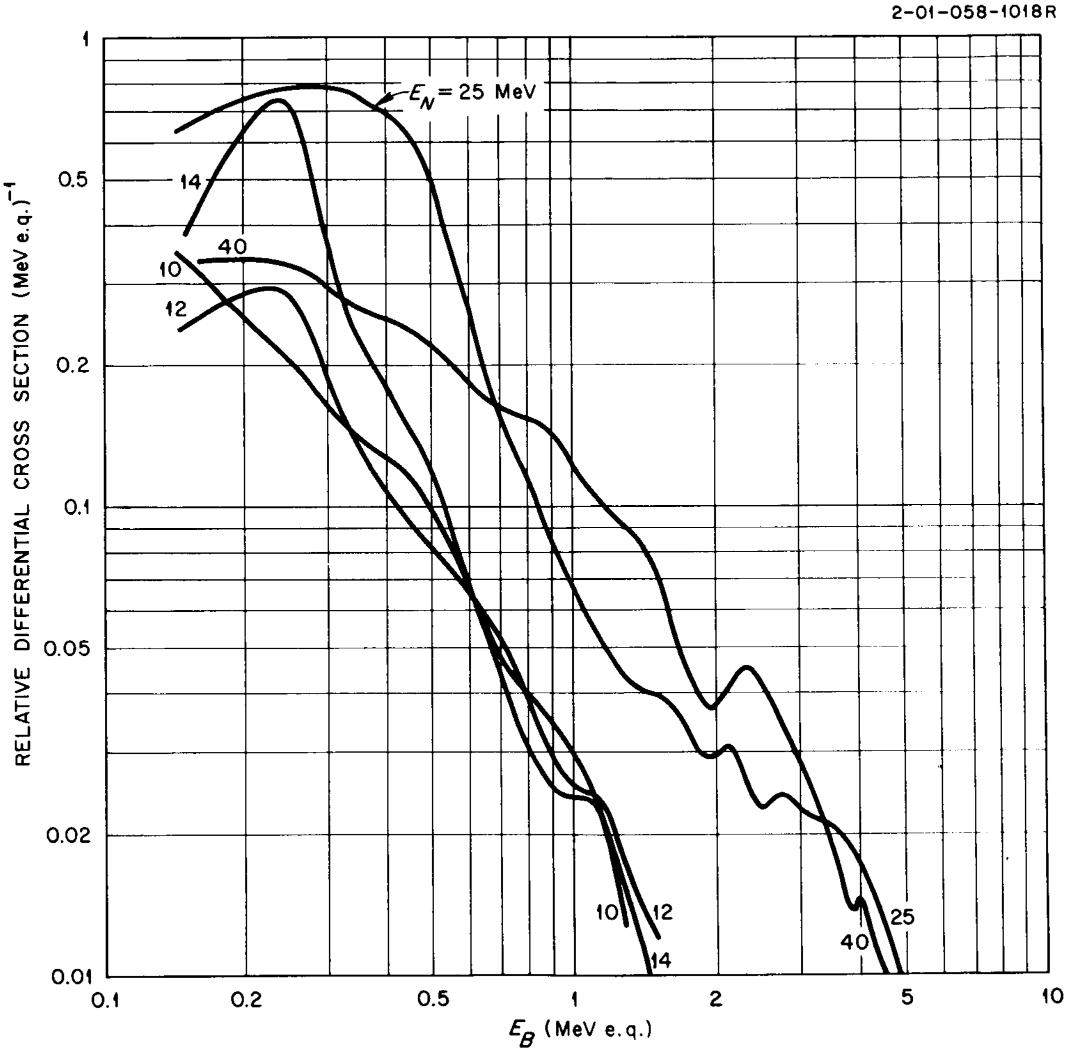

Figure 10. The effective relative differential cross sections for a 2.54-cm-thick NE-213 scintillator as a function of the bias energy (electron equivalent). These data are from R. J. Schuttler, Efficiency of Organic Scintillators for Fast Neutrons, ORNL-3888, July 1966.

the data of Figure 10 which, when combined with the appropriate effective cross section $\Sigma_C^{eff} = N_H\sigma_C^{eff}$ for the cascade reaction, yields a rough estimate of the pulse-height spectrum for the cascade reactions.

To obtain the pulse-height spectrum for the interactions of neutrons of any energy, all that is required is to multiply the ordinate of the "standard" spectrum shown in Figure 11 by the appropriate cross section from Table I, where Table I gives the values for σ_C^{eff} for the reaction as a function of the neutron energy for two detector thicknesses.

The total spectrum. The final step in the derivation of the total pulse-height spectrum is to convert the proton and alpha-particle spectra given by Equations IV-32 and IV-34, respectively, to light-output units.

The fast light-output curves for protons and alpha particles plotted as a function of neutron energy are given in Figure 12. These data are taken from Schuttler[32] and Birks.[33] The light output is measured in terms of an electron which produces the same amount of light as the charged particle being measured. Converting the energy scale for the charged-particle reactions to electron-equivalent light output is accomplished directly from these curves. The cross section at each value of F, however, must be divided by the slope of the light curve where the slope of the curve is given by Birks[34] for the fast light output as

---

[32] Schuttler, op. cit., p. 53.

[33] Birks, op. cit., p. 75.

[34] Ibid.

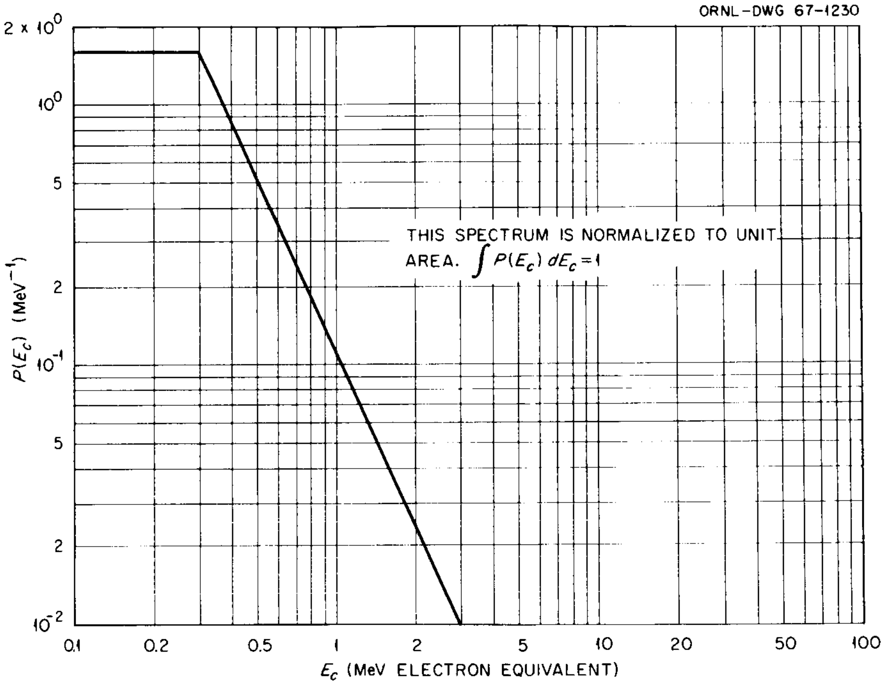

Figure 11. Standard energy spectrum for the carbon cascade spectrum.

TABLE I

EFFECTIVE CROSS SECTION σ_C^{eff} AT E_B = 180 keV. e. q.*

E_N (MeV.)	σ_C^{eff} (mb.) For D = 6.1 cm.	σ_C^{eff} (mb.) For D = 2.54 cm.
10†	94	65
12	128	91
14	187	150
15	207	168
20	319	313
25	326	320
30	334	331
40‡	310	310

---

*These data are from R. J. Schuttler, Efficiency of Organic Scintillators for Fast Neutrons, ORNL-3888, July 1966. E_B is the bias setting of the detector discriminator. 180 keV. electron equivalent (e. q.) corresponds to 1-MeV. neutron energy.

†Below ~7.8 MeV., the cross section goes to zero.

‡For neutron energies greater than 40 MeV. the cross section is nominally 310 mb. for both detectors.

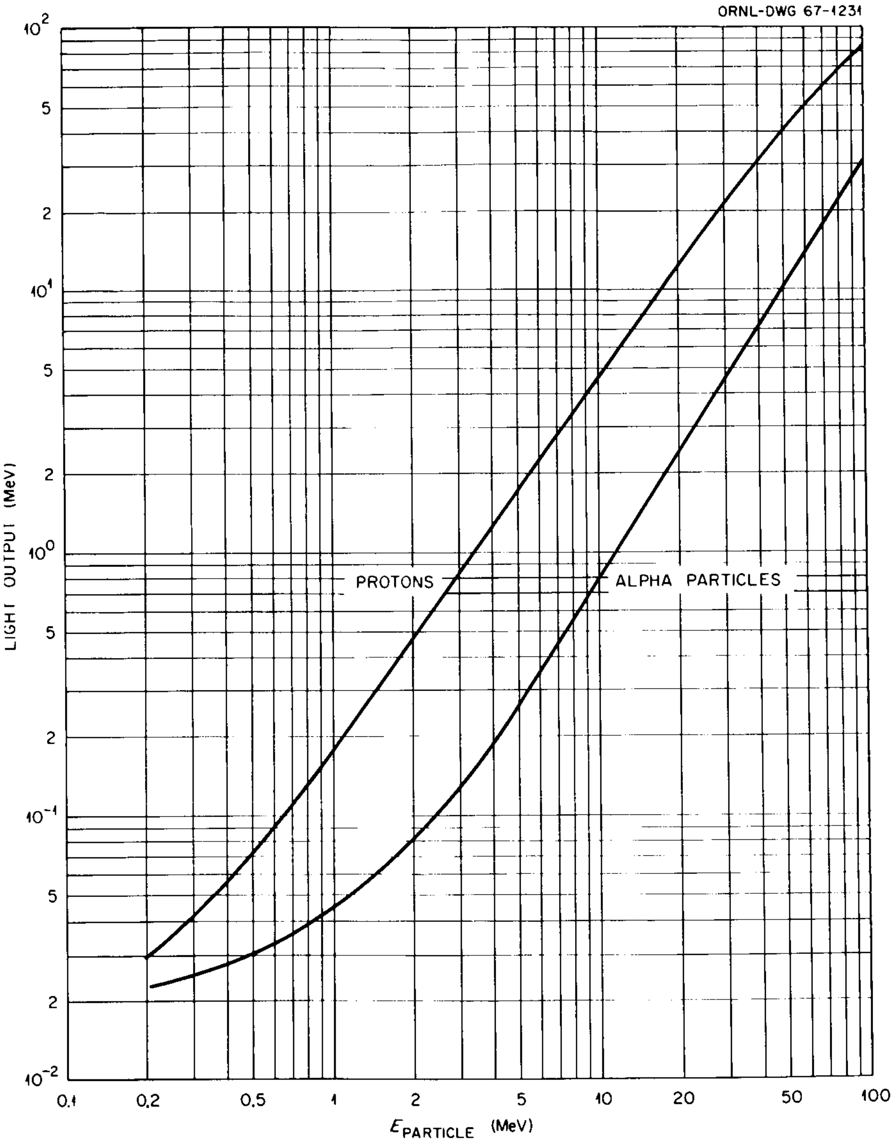

Figure 12. Fast light output for protons and alpha particles.

$$dF/dE = [1 + B(dE/dx)]^{-1} \quad . \qquad \text{IV-35}$$

B is a constant relating the energy loss of the charged particle to the light output (the value of B is taken as 0.0140 g. cm.$^{-2}$ MeV.$^{-1}$ in obtaining the curves in Figure 12) and dE/dx is the energy lost per unit pathlength by the charged particle in passage through the scintillator.

When all the spectral data have been converted to electron-equivalent light-output units (cm.$^{-1}$ MeV.$^{-1}$ electron equivalent) all that remains is to add the proton recoil and alpha-particle spectra with the cascade spectrum. Figure 13 shows the resulting pulse-height spectra for the interactions of 2- and 14.5-MeV. neutrons in the NE-213 scintillator. Also shown is the bias setting for 1-MeV. neutrons. Plotted for the purpose of comparison is the 14.5-MeV. spectra determined experimentally by Love et al.[35]

Conversion to Time Coordinates

The time-slewing response function is obtained by converting the total pulse-height spectrum to time coordinates using the time-slewing curve. In this analysis, we are using the time-slewing curve of Peelle and his coworkers[36] which is modified to be consistent with the definitions of the neutron flight time discussed in Chapter II. The time-slewing curve, shown in Figure 14, plots the ratio of the pulse height

---

[35] T. A. Love et al., Absolute Efficiency Measurements of NE-213 Organic Phosphors for Detecting 14.4- and 2.6-MeV. Neutrons, ORNL-3893, September 1966.

[36] R. W. Peelle et al., Differential Cross Sections for the Production of Protons in the Reactions of 160-MeV. Protons on Complex Nuclei, ORNL-3887, September 1966.

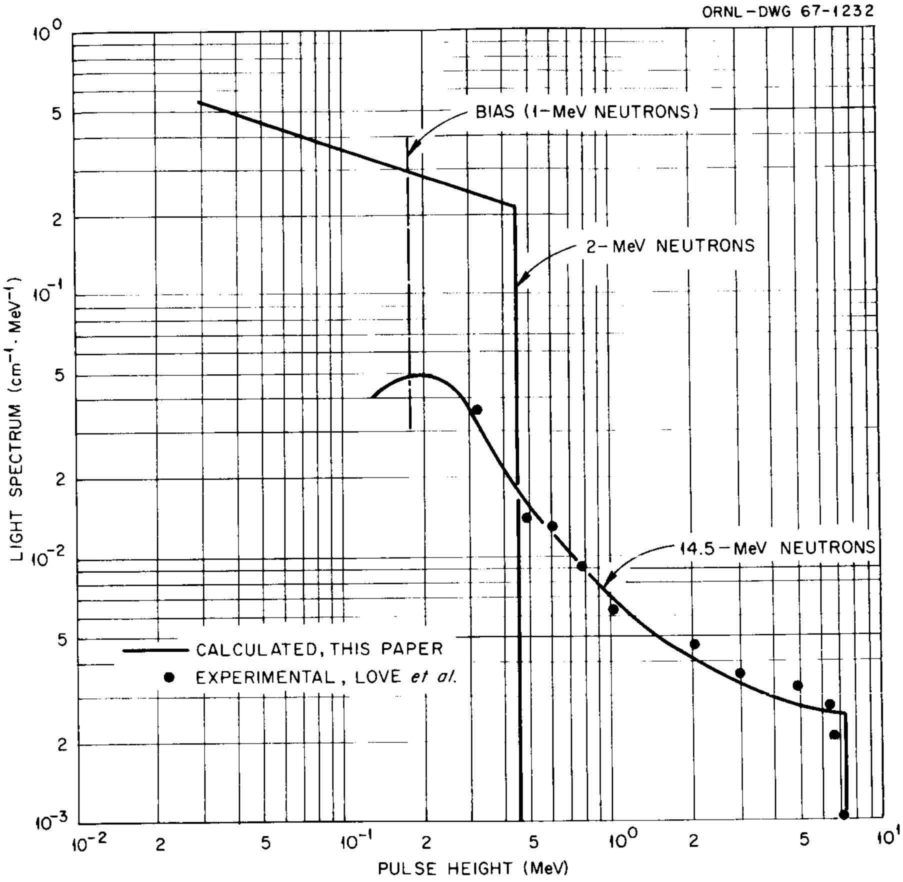

Figure 13. Fast-light pulse-height spectrum per centimeter for 2- and 14.5-MeV. neutrons.

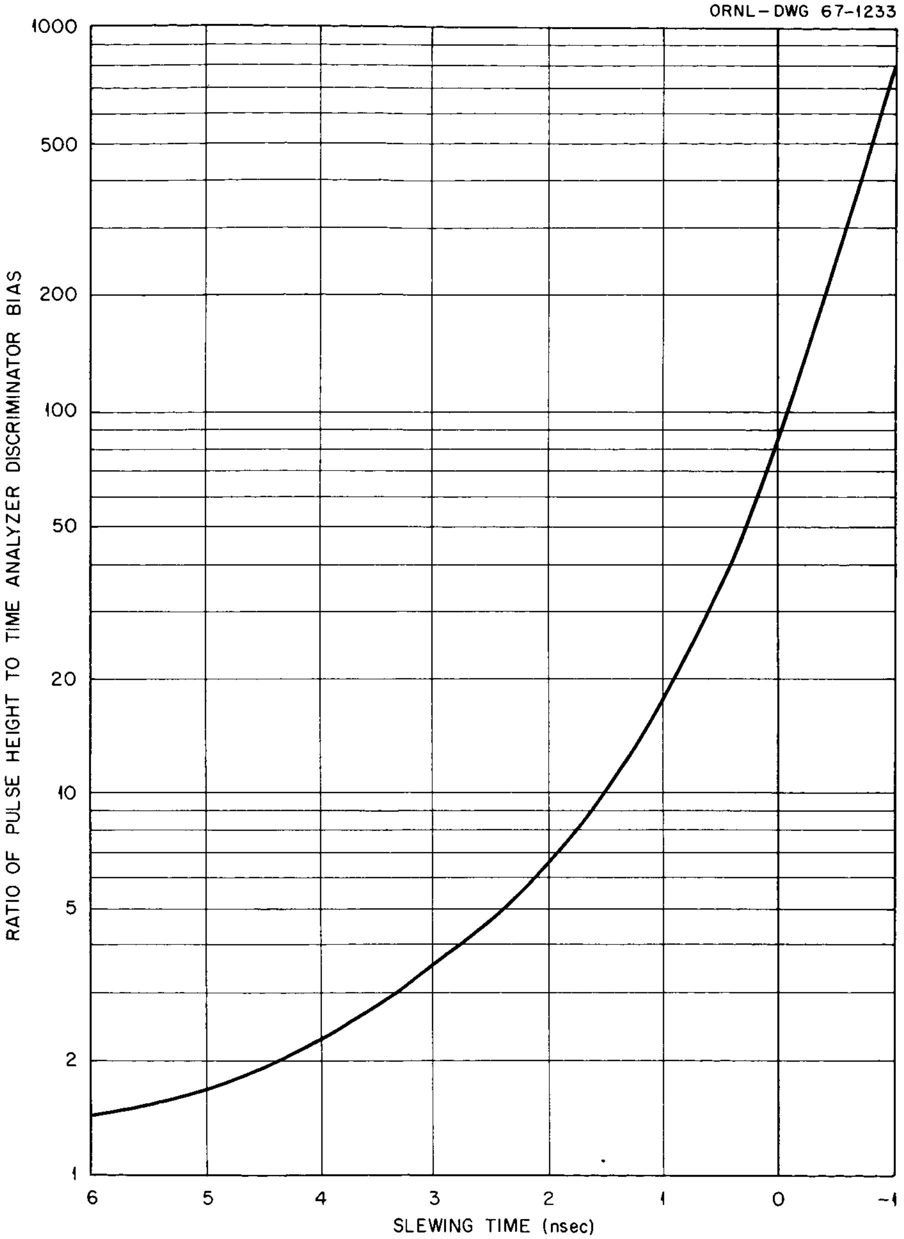

Figure 14. The time-slewing curve for the neutron detector. These data are from R. W. Peelle et al., ORNL Report No. 3887. For this analysis the data have been modified to be consistent with the definitions for the time and may appear reversed when compared with the original data.

to the time analyzer discriminator trigger level as a function of the time shift or slewing.

The zero slewing time shown in the figure is taken arbitrarily. In an experiment, this zero value must be determined specifically for the detector and instrumentation being used. The "zero" flight time is initially established from measurements of the apparent flight time of the highest energy particle available. For experiments of the type being studied here, the proton beam is usually used. The time slewing as a function of the pulse amplitude for constant flight time is then measured and the zero time slewing is assigned for pulses of the same amplitude as those occurring during the determination of "zero" flight time.

Converting the pulse-height spectrum to time coordinates is a straight-forward process. The pulse height (abscissa of Figure 13) is initially divided by the discriminator bias setting, taken here to be 90 keV., and the corresponding time slewing is read directly from Figure 14. The ordinate of the pulse-height spectrum is then multiplied by the slope of the walk curve where the slope is defined in units of (MeV./nsec.).

Figure 15 shows the slewing response function for 2- and 14.5-MeV. neutrons. These data have been normalized to unity consistent with the definition given by Equation IV-31. The abscissa is in units of time and the ordinate in reciprocal time units. It should also be noted that both curves show a maximum slewing time of 4.3 nsec. This corresponds to the walk at a detector bias setting of 1 MeV. for neutrons (180-keV. electron equivalent); the value of the bias used in all calculations.

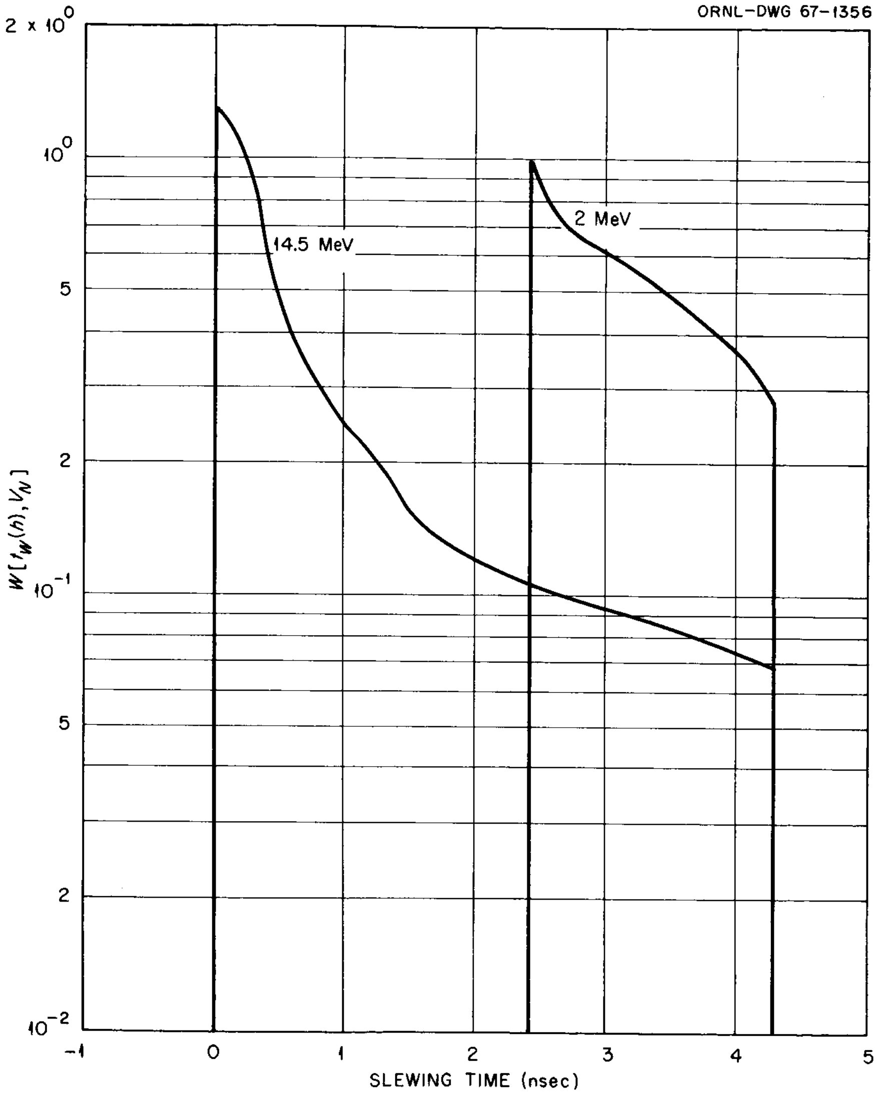

Figure 15. The time-slewing response functions $W[t_w(h), v_n]$ for 2- and 14.5-MeV. neutrons as a function of the slewing time.

V. THE TIME-ANALYZER RESPONSE FUNCTION

The time-analyzer response functions are the probability that a neutron of measured flight time t_m (see Equation II-5) produces a count in channel k of the multichannel time analyzer. The analyzer response function is approximated by a rectangular distribution over the width of a time channel by

$$A_k(t_m) = \begin{cases} 1; & n\left(k - \frac{1}{2}\right) < t_m \le n\left(k + \frac{1}{2}\right) \\ 0; & \text{otherwise} \end{cases} \qquad \text{IV-36}$$

where n is the analyzer conversion gain in nsec./channel.

VI. INTEGRALS LEADING TO THE TIME-CHANNEL RESPONSE FUNCTION

The probability per MeV. of neutron energy per incident proton that a neutron of speed v_n is detected in channel k of the multichannel time analyzer is the time-channel response function and is given by the expression

$$S_k(v_p;v_n,\theta) = \int_{t_m} A_k(t_m)\, T(v_p;v_n,t_m)\, dt_m \qquad \text{IV-37}$$

where $A_k(t_m)$ are the time-analyzer response functions and $T(v_p;v_n,t_m)\, dt_m$ is the probability per incident proton per MeV. of neutron energy that a neutron of speed v_n has a measured flight time within dt_m at t_m. $T(v_p;v_n,t_m)$ is obtained from the convolution of the flight-time distribution of detected neutrons averaged over the target volume, $C(v_p;v_n,t_i)$, and the time-slewing response function, $W[t_w(h),v_n]$, given by

$$T(v_p;v_n,t_m) = \int_{t_i} C(v_p;v_n,t_i)\, W(t_m - t_i,v_n)\, dt_i \quad , \qquad \text{IV-38}$$

where $t_w(h) = t_m - t_i$ from Equations II-5 and IV-13.

The summation of $S_k(v_p;v_n,\theta)$ over all the time channels yields the average detector efficiency $\overline{\epsilon_D(v_n)}$ times the number of neutrons which strike the detector given by Equation IV-30. With the aid of Equation IV-36, we can write Equation IV-37 as

$$\sum_k S_k(v_p;v_n,\theta) = \sum_k \int_{n[k-(1/2)]}^{n[k+(1/2)]} 1 \cdot T(v_p;v_n,t_m)\, dt_m \quad . \qquad \text{IV-39}$$

Using the same arguments which led to Equation IV-21, it can be shown that

$$\int_{t_m} T(v_p;v_n,t_m)\, dt_m = \int_{t_i} C(v_p;v_n,t_i)\, dt_i \quad . \qquad \text{IV-40}$$

Introducing the results from Section III for the integral of $C(v_p;v_n,t_i)$ over the jitter-smeared flight time, we obtain the result

$$\sum_k S_k(v_p;v_n,\theta) = \overline{\epsilon_D(v_n)}\, \Sigma_p(v_p;v_n,\theta)\left[\frac{1}{\Sigma_{TP}^{eff}}\right]\left[1 - e^{-\Sigma_{TP}^{eff}\, S}\right]\Delta\Omega_o \quad . \qquad \text{IV-41}$$

CHAPTER V

COMPUTATION OF THE TIME-CHANNEL RESPONSE FUNCTION

The equations leading to the time channel response function discussed in Chapter IV are sufficiently complex that a computer was required to facilitate the computations. Four computer programs were written, each designed to complete a separate phase of the analysis. These programs are discussed briefly in Figure 16 which shows, in block diagram, how they are combined to produce the desired response functions. In this chapter, the methods of analysis used in each program will be discussed along with some of the particular calculations which are necessary to understand the solution of the problem. The specific details and descriptions of the programs and instructions for their use are given elsewhere.[37]

I. THE NUMERICAL CALCULATION OF THE JITTER-SMEARED PHYSICAL FLIGHT-TIME DISTRIBUTION OF DETECTED NEUTRONS

The numerical calculation of the jitter-smeared physical flight-time distribution was accomplished by completing the integration shown in Equation IV-15 and evaluating the results at values of t_i for which the distribution is nonzero. The integration was performed using Gaussian quadratures with all computations being performed on a Control Data Corporation 1604 Computer.

---

[37] R. T. Santoro, A Fortran Program for Calculating the Time Channel Response Function in Neutron Time-of-Flight Spectroscopy; to be published.

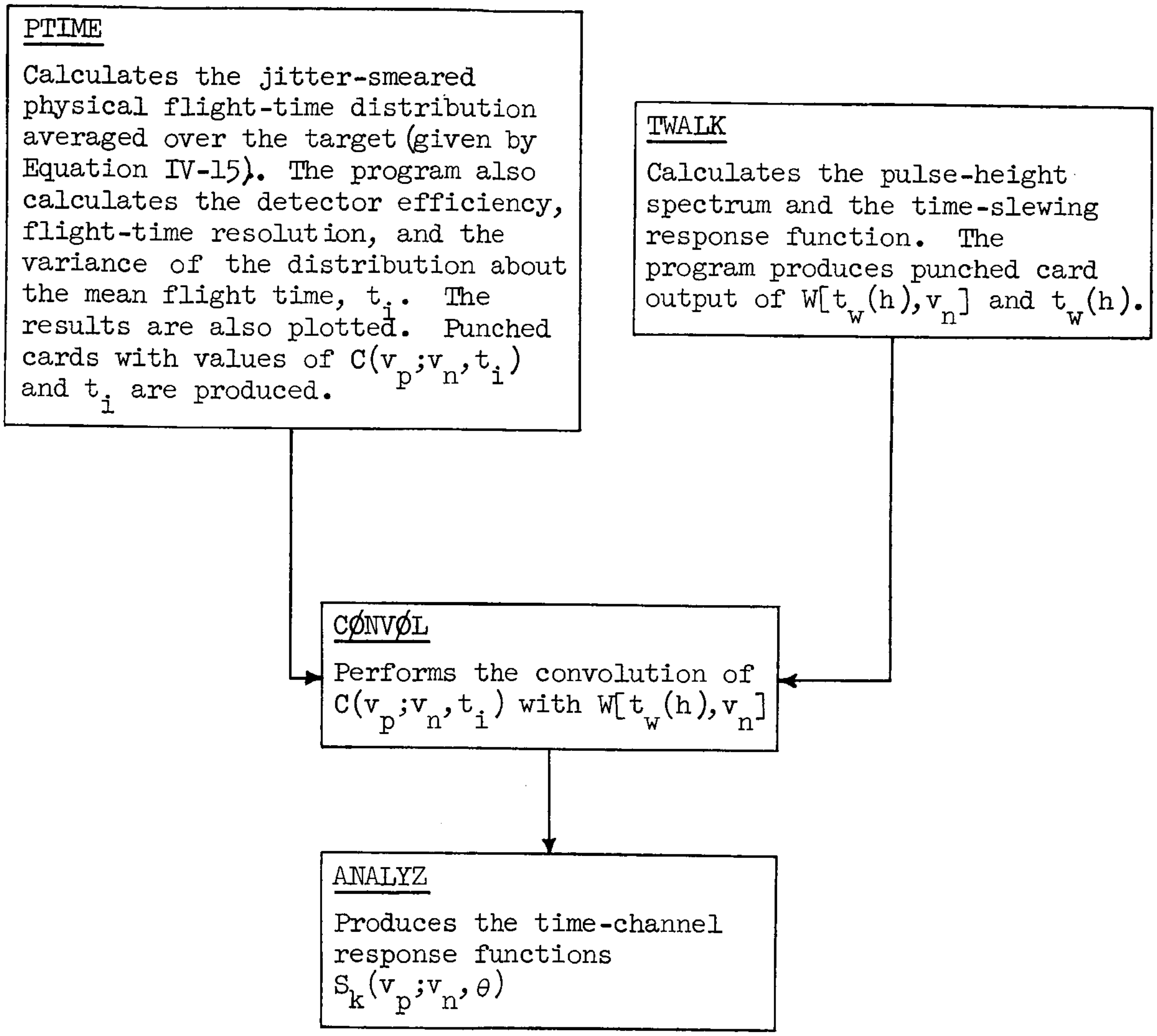

PTIME

Calculates the jitter-smeared physical flight-time distribution averaged over the target (given by Equation IV-15). The program also calculates the detector efficiency, flight-time resolution, and the variance of the distribution about the mean flight time, t_i. The results are also plotted. Punched cards with values of $C(v_p;v_n,t_i)$ and t_i are produced.

TWALK

Calculates the pulse-height spectrum and the time-slewing response function. The program produces punched card output of $W[t_w(h),v_n]$ and $t_w(h)$.

CØNVØL

Performs the convolution of $C(v_p;v_n,t_i)$ with $W[t_w(h),v_n]$

ANALYZ

Produces the time-channel response functions $S_k(v_p;v_n,\theta)$

Figure 16. Block diagram and description of the computer programs for calculating the time-channel response function.

Detailed discussions of the Gaussian quadrature procedure are given by Lanczos[38] and Kou.[39] This method of integration was chosen since it yields an accurate approximation to the integral and requires fewer computational steps than other methods. In this section, we shall discuss the more important aspects of the calculations and some of the criteria used to evaluate the results.

Tabulation of Cross Sections

The calculations made in this analysis were based on the use of a carbon target and an NE-213 scintillator. The assumption was made that the effective macroscopic cross section for neutron absorption in the target is zero. For thin targets, in which the neutron mean free path is much greater than the distance travelled by the neutron from the (p,n) interaction point to the point of exit from the target, the assumption is quite reasonable. For example, for 2-MeV. neutrons the total cross section for carbon is ~1.7 b. and the corresponding mean free path is ~7.5 cm.

The effective macroscopic cross section for neutrons in the detector was obtained from

$$\Sigma_D^{eff} = N_H\sigma_H + N_C\sigma_{C,ne} \quad , \qquad \text{V-1}$$

where N_H and N_C are the atomic densities of hydrogen and carbon in the detector, σ_H is the microscopic total cross section for hydrogen, and

---

[38] Cornelius Lanczos, Applied Analysis, (Prentice Hall, Inc., Englewood Cliffs, New Jersey, 1956), pp. 396-410.

[39] Shan S. Kuo, Numerical Methods and Computers, (Addison-Wesley, Reading, Massachusetts, 1965), pp. 239-252.

$\sigma_{C,ne}$ is the nonelastic microscopic cross section for carbon. Table II lists the values for σ_H and $\sigma_{C,ne}$ over the range of neutron energies from 2 to 100 MeV.

The macroscopic efficiency cross section $\Sigma(v_n)$ was taken from Schuttler.[40] These data are based on first collision calculations of the detector efficiency for bias values of 180-keV. electron equivalent. This corresponds to 1 MeV. for neutrons. Schuttler's data extend up to 50 MeV. For higher neutron energies, the efficiency cross section was inferred from the total hydrogen and carbon cross sections. Figure 17 is a curve of $\Sigma(v_n)$ versus neutron energy. Also shown in the figure are macroscopic cross sections for hydrogen and carbon which contribute to the efficiency cross section.

The macroscopic absorption cross section for protons in the target Σ_{TP}^{eff} was estimated using the nonelastic cross section for neutrons in carbon from the data of Bertini.[41] σ_{TP}^{eff} was taken as 233 mb. This value compares favorably with the value given by Voos and Wilson of 225 mb.[42]

Reduction of the Integral to Quadratures

The evaluation of Equation IV-15 requires the solution of a four-fold integral evaluated at the values of the jitter-smeared apparent flight-times t_i for which the distribution is nonzero. The range of flight times for which the distribution is nonzero is implied by the conditions of

---

[40] R. S. Schuttler, Efficiency of Organic Scintillators to Fast Neutrons, ORNL-3888, July 1966.

[41] H. Bertini, Phys. Rev. 131, 1801 (1963).

[42] R. G. P. Voos and R. Wilson, Proc. Roy. Soc. (London), A236, 41 (1956).

TABLE II

VALUES OF σ_H AND $\sigma_{C,ne}$ FOR $2 \leq E_N \leq 100$ MeV.

E_N MeV.	σ_H[*] barn	$\sigma_{C,ne}$[†] barn
2	2.90	1.72
5	1.63	1.15
10	0.94	0.64
15	0.65	0.87
20	0.48	1.04
25	0.38	0.92
30	0.31	0.87
35	0.26	0.82
40	0.22	0.76
50	0.17	0.64
60	0.13	0.53
70	0.10	0.43
80	0.09	0.35
90	0.08	0.30
100	0.07	0.26

[*] Neutron Cross Sections, BNL-325, Second Edition, Brookhaven National Laboratory, February 1966.

[†] M. Kalos and H. Goldstein, Neutron Cross-Section Data for Carbon, NDA 12-16 (1956).

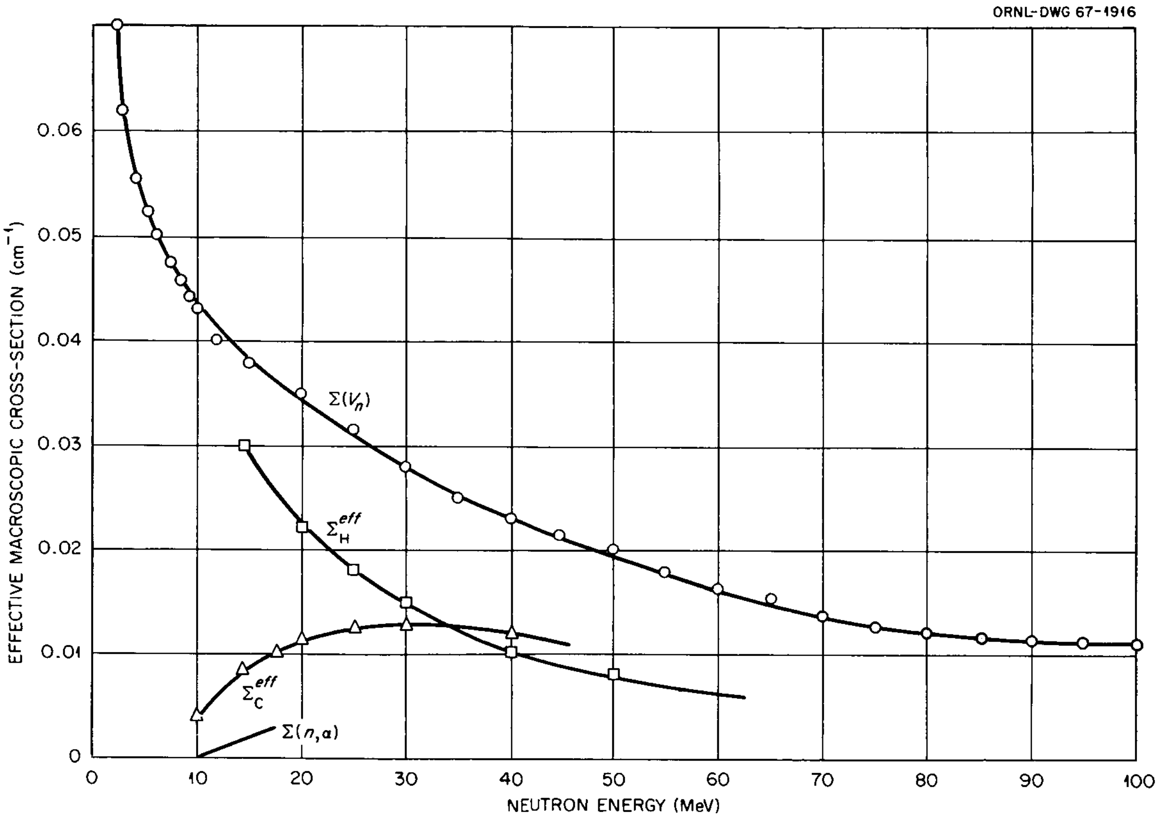

Figure 17. First-collision effective macroscopic cross sections as a function of neutron energy. The bias energy is 180-keV. (electron equivalent.) which corresponds to 1 MeV. for neutrons.

Equation IV-4. The values of t_i used in the evaluation of the integral were determined from the extremum flight paths for the neutron for the particular target-detector geometry being studied. The minimum and maximum flight times were defined by $(t_i)_{min} = (\ell_f)_{min}/v_n - 2.5\sigma_j$ and $(t_i)_{max} = (\ell_f)_{max}/v_n + 2.5\sigma_j$ where $(\ell_f)_{min}$ and $(\ell_f)_{max}$ are the extremum flight paths for the neutron between the target and the detector and σ_j is standard deviation of the jitter distribution. The addition and subtraction of $2.5\sigma_j$ insures that the values of t_i are defined well into the region of the tails of the jitter smeared distribution. The time mesh was then taken in equal intervals between $(t_i)_{min}$ and $(t_i)_{max}$.

The integral over the face of the detector was evaluated by expressing the element of detector area in terms of the cylindrical coordinates on the face of the detector. Then

$$dA_D = \rho d\rho d\alpha \qquad \text{V-2}$$

where ρ and $d\rho$ are the radial components and $d\alpha$ is the element of azimuthal angle. The integration over the face of the detector was broken down into two regions in order to take into account the effects of the detector edges. The contributions to the flight-time distribution were then added according to their respective weights and the integral was evaluated over α as follows

$$2\int_{-\pi/2}^{\pi/2}\int_0^{R_D} \rho d\rho d\alpha = 2\int_{-\pi/2}^{\pi/2} d\alpha \left[\int_0^{R_D'(\alpha)} \rho d\rho + \int_{R_D'(\alpha)}^{R_D} \rho d\rho\right] \qquad \text{V-3}$$

where R_D' is the value of the radius for which the projected flight-path of the neutron along $\vec{\Omega}$ just intercepts the point where the rear surface and the cylindrical surface intersect. The factor of two in the integration is required since the integrals are evaluated over half of the detector. The integration over the target volume is straightforward; the limits of integration for x and y being given previously by Equations IV-28 and IV-29.

The most tedious problem faced in computing the results was the determination of the proper number of quadrature points required in the integration. This was accomplished in several ways. First, the results were normalized to the calculated area under the Gaussian beam distribution; the area being evaluated using the same number of quadrature points as in the integral over y. This procedure reduced the sensitivity of the distribution to the number of quadrature points in y. Then, the area of the detector face was inspected for a given number of quadrature points in ρ and α. If the computed area was the same as the known area of the detector face, the computation was allowed to proceed.

These steps, however, did not always yield the optimum approximation to the solution of the equation. The use of very narrow jitter distributions, where σ_j was small compared to Δt_i, sometimes required a larger number of quadrature points and/or a tighter time mesh. Often, the best results were reached by trial and error and the correct number of quadrature points was determined when the value for the integral converged and increasing the number of points no longer affected the results.

Testing the Validity of the Results

After inspecting the results to insure that the solution to the integral had converged, the resulting jitter-smeared flight-time distribution was integrated over all values of t_i to obtain the detector efficiency. The solution was assumed correct if the efficiency calculated in this manner compared to the efficiency calculated from Equation IV-23. This equation was computed using the values for the maximum and minimum flight times used to obtain the distribution.

II. NUMERICAL CALCULATION OF $T(v_p;v_n,t_m)$

The jitter-smeared physical flight-time distribution and the time-slewing response function were convoluted as shown in Equation IV-38 using trapezoidal quadratures in Program CØNVØL. In this calculation, the time-slewing distribution was divided into equal time intervals such that the initial and final time-slewing values formed the upper and lower time limits. The physical flight-time distribution was then divided into intervals of the same size. Forming the intervals in this manner insured that the edges of the time-slewing distribution (see Figure 15) were properly represented in the quadrature.

III. INTERPOLATION AND ENTABULATION

In this analysis, we have made wide use of the TERP code of Putzulu *et al.*[43] This code enables the user to make rapid accurate numerical approximations to functions which are not normally provided in the computer library.

All of the cross-section curves and tables of the error function were approximated using this system. The system yields specific values for these approximated functions by parabolic interpolation within the tabulated values supplied to the system.

---

[43] D. T. Putzulu, P. Aebersold, and W. R. Burrus, *Description of the TERP System, A Fortran II/63, IV/63, 360 System for Efficient Interpolation*, ORNL-TM-1706 (December 8, 1966).

CHAPTER VI

RESULTS

In this chapter, we shall present some typical results from the numerical solutions of the equations presented in the preceeding chapters. Some characteristic jitter smeared physical flight-time distributions of detected neutrons averaged over the target will be illustrated for the interactions in the detector of 2-, 14.5-, and 100-MeV. neutrons and the effects on these distributions arising from the instrumental time jitter will be demonstrated.

Comparisons will be made between the maximum flight-time uncertainties induced by the target and detector dimensions using the equations derived in Chapter III and the uncertainties predicted by the computed flight-time distributions for the same conditions. Finally, the effects on the flight-time distributions arising from the convolution with the time-slewing response function will be discussed and some typical time-channel response functions will be presented.

I. COMPUTED PHYSICAL FLIGHT-TIME DISTRIBUTIONS

The physical flight-time distributions for detected neutrons averaged over the target were obtained from the numerical integration of Equation IV-15. For the purpose of this analysis, the target-detector configuration and parameters summarized in Table III were chosen to demonstrate the results; these parameters typifying a practical choice

TABLE III

PARAMETERS USED IN COMPUTING THE PHYSICAL FLIGHT-TIME DISTRIBUTION

Proton Beam	Target Orientation	
$E_N = 160$ MeV.	Composition	Carbon
$\sigma = 0.25$ cm.*	Thickness (T)	0.5 cm.
	Rotation Angle (Ψ)	30°
	$\tau_1 + \tau_2$	0

Detector Parameters	
Normal Distance from $x = y = z = 0$ to the Face of the Detector (L)	70 cm.
Neutron Scattering Angle (θ)	60°
Thickness (D)	6.01 cm.
Radius (R_D)	6.0 cm.
Index of Refraction (K)	1.43

---

*Based on measured values used in the parent experiment. See R. T. Santoro, The Space, Time, and Energy Distributions of the Proton Beam of the Harvard University Synchrocyclotron, ORNL-3722 (January 1965).

in the light of possible experimental arrangements for the target and detector.

The distributions were approximated using four-point Gaussian quadratures in x, y, ρ, and α with a 40-point mesh in t_i for secondary neutron energies of 2-, 14.5-, and 100-MeV. The results of the computation are shown in Figure 18 for the cases where $\sigma_j = 0.43$ and 0.86 nsec. The abscissa gives the jitter smeared apparent physical flight time and the ordinate is the probability per incident proton per MeV. of neutron energy that a secondary neutron of speed v_n has an apparent jitter smeared flight time per nsec. at t_i. The ordinate values have been divided by the effective target thickness, the detector solid angle, and $\Sigma_p(v_p;v_n,\theta)$. The resulting distributions have been normalized to the computed area under the beam distribution.

All of the distributions with the exception of the one computed for 2-MeV. neutrons with $\sigma_j = 0.43$ nsec. are essentially Gaussian in nature with the chief contribution to the time spread arising from the instrumental jitter. For example, at 14.5 MeV, the mean flight time for the neutrons over the 70-cm. flight path is 14.15 nsec. The resolution time assuming only presence of the jitter is 7.1% and 14.2% when $\sigma_j = 0.43$ and 0.86 nsec., respectively.

For the single case where $E_n = 2.0$ MeV. with $\sigma_j = 0.43$ nsec. the shape of the distribution is obviously different. The sloping character of the top edge of the distribution is the result of neutron attenuation in the detector; the attenuation being of the order of $e^{-.84}$.

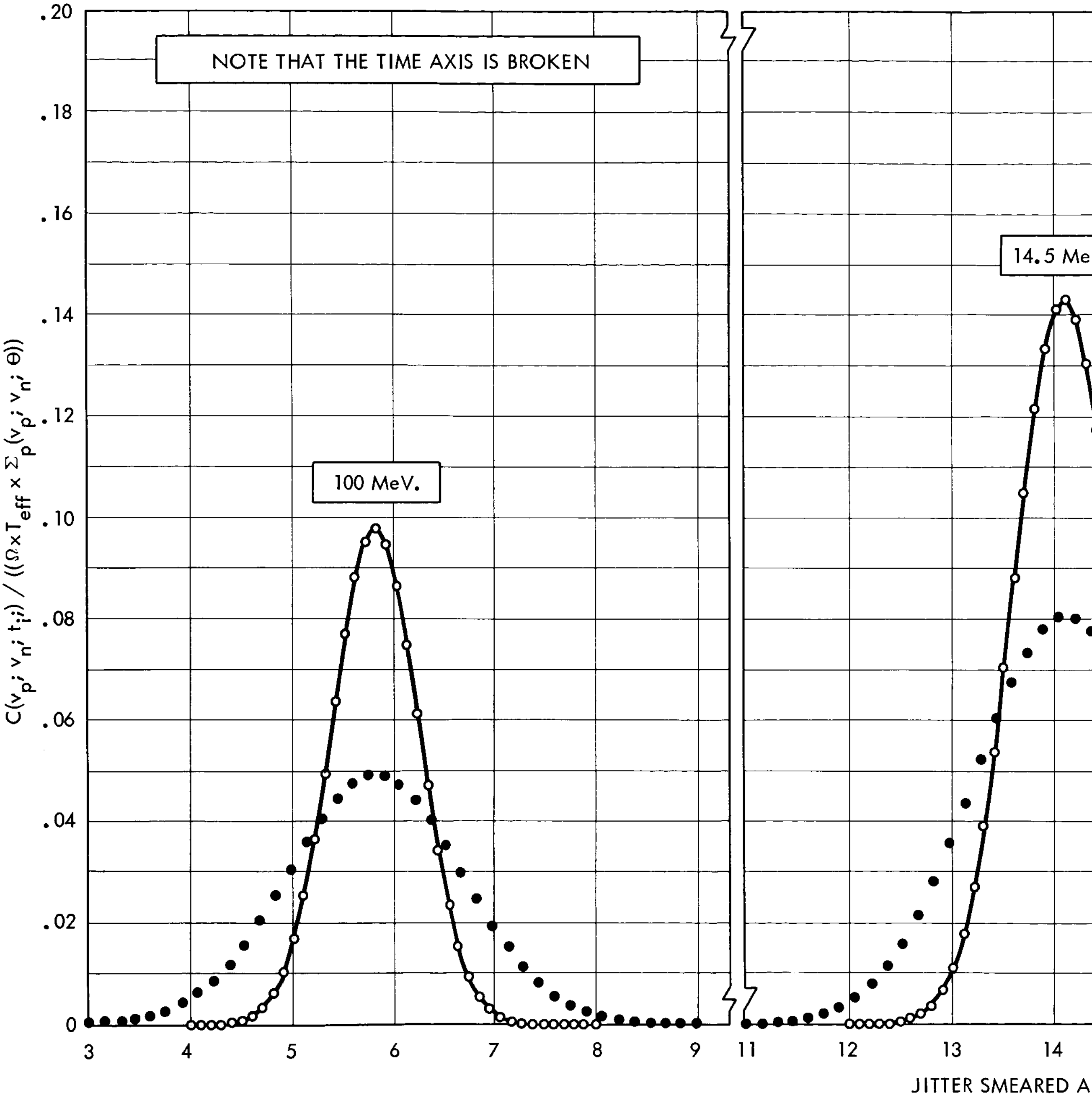

Figure 18. Flight-time
neutrons for a 6.01-cm.-thick
$\theta = 60^\circ$, and $\Psi = 30^\circ$. The resul
shown.

75-2

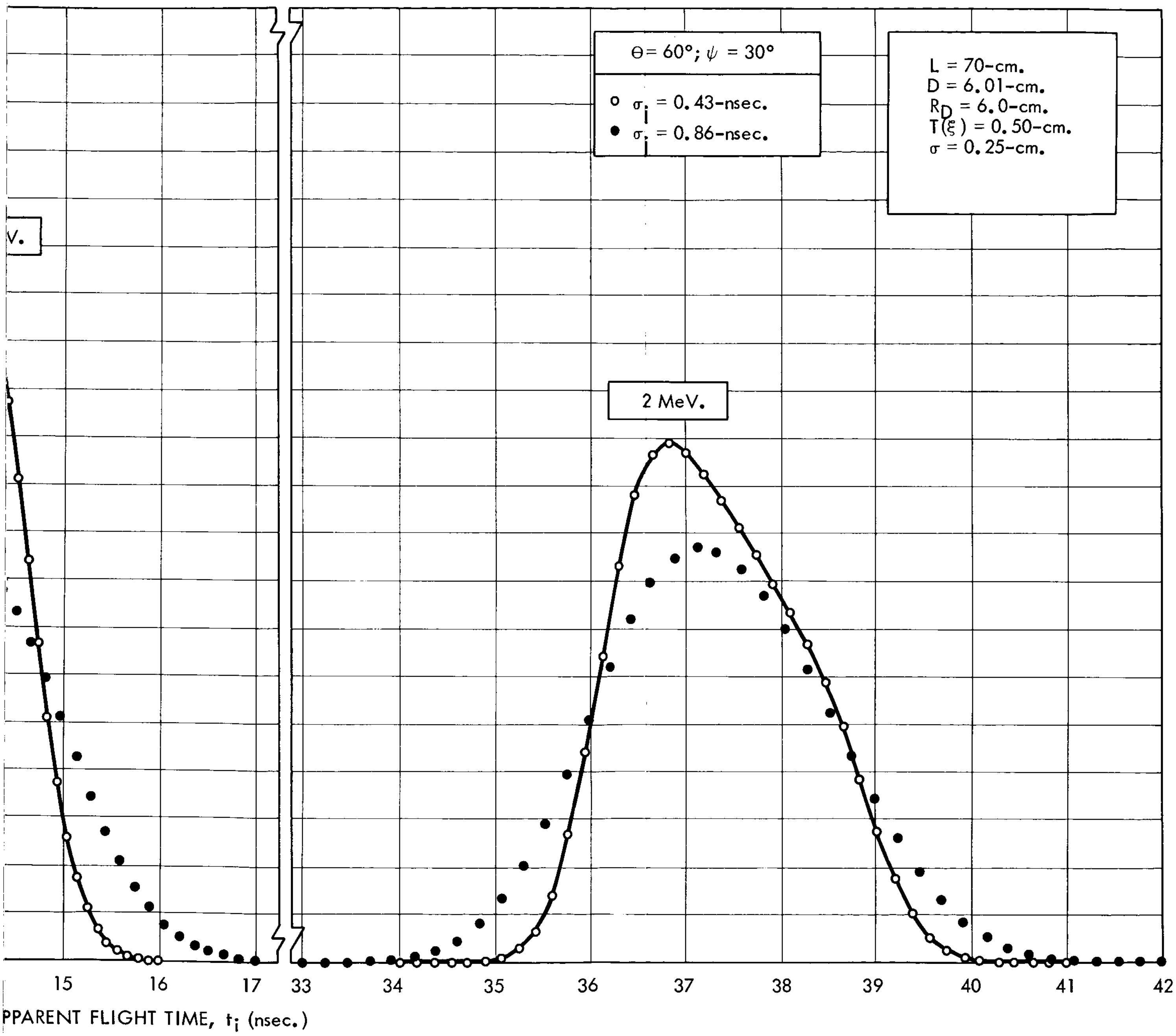

distributions for 2-, 14.5-, and 100-MeV.
letector. For these data L = 70 cm.,
lts for σ_j = 0.43 and 0.86 nsec. are

The results of these calculations are summarized further in Table IV. The detection efficiencies, obtained from the integral of the flight-time distribution over the range of flight times, are compared to the experimental values of Love et al.,[44] for a detector of approximately the same size. The differences in the values listed result primarily from the single scattering approximation used in this calculation to estimate the pulse-height spectrum.

Improving the timing resolution for the configuration may be accomplished by increasing the flight path. For example, for L = 200 cm., the overall timing resolution reduces by a factor of 2.7 which corresponds approximately to the increase in the flight time. There is, however, a corresponding decrease in the system efficiency arising from the reduction in solid angle subtended by the detector, and increased counting times would be required to gain comparable statistical accuracy in experimental data.

It should also be noted that the values for the geometric resolution given in Table IV differ. This arises since the jitter was subtracted in quadrature. This technique does not represent a precise way of eliminating this effect.

II. COMPARISONS WITH CALCULATED FLIGHT-TIME UNCERTAINTIES

The maximum relative flight-time uncertainties introduced by the target and detector dimensions were calculated in Chapter III under the

---

[44] T. A. Love et al., Absolute Efficiency Measurements of NE-213 Organic Phosphors for Detecting 14.4- and 2.6-MeV. Neutrons, ORNL-3893, September 1966.

TABLE IV

RESULTS FROM THE COMPUTATION OF

$C(v_p;v_n,t_i)/[\Omega\ T_{eff}\ \Sigma_p(v_p;v_n,\theta)]$

VERSUS t_i

E_N (MeV.)	$\langle t_i \rangle$ (nsec.)	FWHM* (nsec.)	GFWHM† (nsec.)	Total Time Resolution (%)	Geometric Resolution (%)
		$\sigma_j = 0.43$ nsec.			
2	37.3	2.51	2.29	6.7	6.1
14.5	14.1	1.19	0.63	8.5	4.5
100	5.8	1.02	0.13	17.5	2.3
		$\sigma_j = 0.86$ nsec.			
2	37.3	2.92	2.11	7.8	5.7
14.5	14.1	2.11	0.61	15.0	4.3
100	5.8	2.03	0.15	34.8	2.5

E_N (MeV.)	Computed Efficiency	Efficiency from Love‡	Zero Bias Efficiency**
2	28.5	38.5	56.9
14.5	18.1	22.6	27.8
100	6.5		7.2

*FWHM is full width at half maximum.

†GFWHM is $[(\text{FWHM})^2 - (2.354 \times \sigma_j)^2]^{1/2}$.

‡T. A. Love et al., Absolute Efficiency Measurements of NE-213 Organic Phosphors for Detecting 14.4- and 2.6-MeV. Neutrons, ORNL-3893, September 1966.

**These data are the same for $\sigma_j = 0.43$ and $\sigma_j = 0.86$.

PRECEDING PAGE BLANK NOT FILMED.

assumption that all the dimensions have negligible effect except the one being evaluated. In order to approximate these same conditions in the computation of the physical flight-time distributions for a given dominant target or detector dimension, the remaining dimensions were made sufficiently small that their combined contribution to the flight-time distribution was small. The computer program logic prohibited their being set equal to zero.

The numerical calculation of $C(v_p;v_n,t_i)$ is dependent on the existence of some fraction of instrumental time jitter. Recalling Equation IV-15, we note that σ_j, the standard deviation of the jitter distribution, enters the calculation of the flight-time distribution principally through the evaluation of the two error functions. For σ_j approaching zero, the difference between the error functions varies between 0 and 1 for combinations of quadrature points in the target and detector and the computed flight-time distribution "oscillates" with t_i Since it is not possible then to use zero jitter, σ_j was made sufficiently small that the full width of the jitter distribution was small compared to the full width at half maximum (FWHM) of the underlying "geometric" component of the flight-time distribution. The value of σ_j used in a given calculation was determined from estimates of the difference in the maximum and minimum flight times along a given direction $\vec{\Omega}$. If the range of neutron flight times were such that the value of $(t_{max} - t_i)/\sigma_j$ and $(t_{min} - t_i)/\sigma_j$ were greater than 4.215, the difference in the error function was zero and the distribution goes to zero over this time region. Since the numerical calculation of the physical flight-time distribution is sensitive to σ_j, the optimum value was often determined by observing the behavior of $C(v_p;v_n,t_i)$ as a function of σ_j.

Figure 19 shows the flight-time resolution, $(\Delta t/t)$ induced by the detector geometry as a function of R_D/L and D/L. The flight-time resolution was obtained from the ratio of the full width of half maximum (FWHM) to the calculated mean flight time, $\bar{t}_i$, of the distribution; the instrumental timing resolution component having been removed.

Eliminating the effects of the jitter was accomplished in two ways. If the width of the jitter distribution, given by 2.36 σ_j, was less than 10% of the width of the combined jitter and geometric distributions, it was subtracted in quadrature. This method gives an imperfect result since the "geometric" component of the distribution is rectangular rather than Gaussian.

The rectangular shaped distribution arises, in the case of the detector thickness, for the following reasons. In the absence of any neutron attenuation and with insignificant target dimensions, the probability for neutron detection given by Equation IV-4 reduces to

$$dt\ I(t,v_n,\vec{\Omega}) = \Sigma(v_n)\ d\ell_D(t) \quad . \qquad \text{VI-1}$$

For $\ell_D(t)$ inconsistent with neutron detection in the detector, $I(t,v_n,\vec{\Omega})$ is zero. Otherwise, I is proportional to $\Sigma(v_n)$ for all values of $\ell_D(t)$ and the resulting distribution is flat across the range of allowed values of t. When the neutron attenuation cross section is introduced, the rectangular-shaped distributions reduces to a trapezoid as shown in

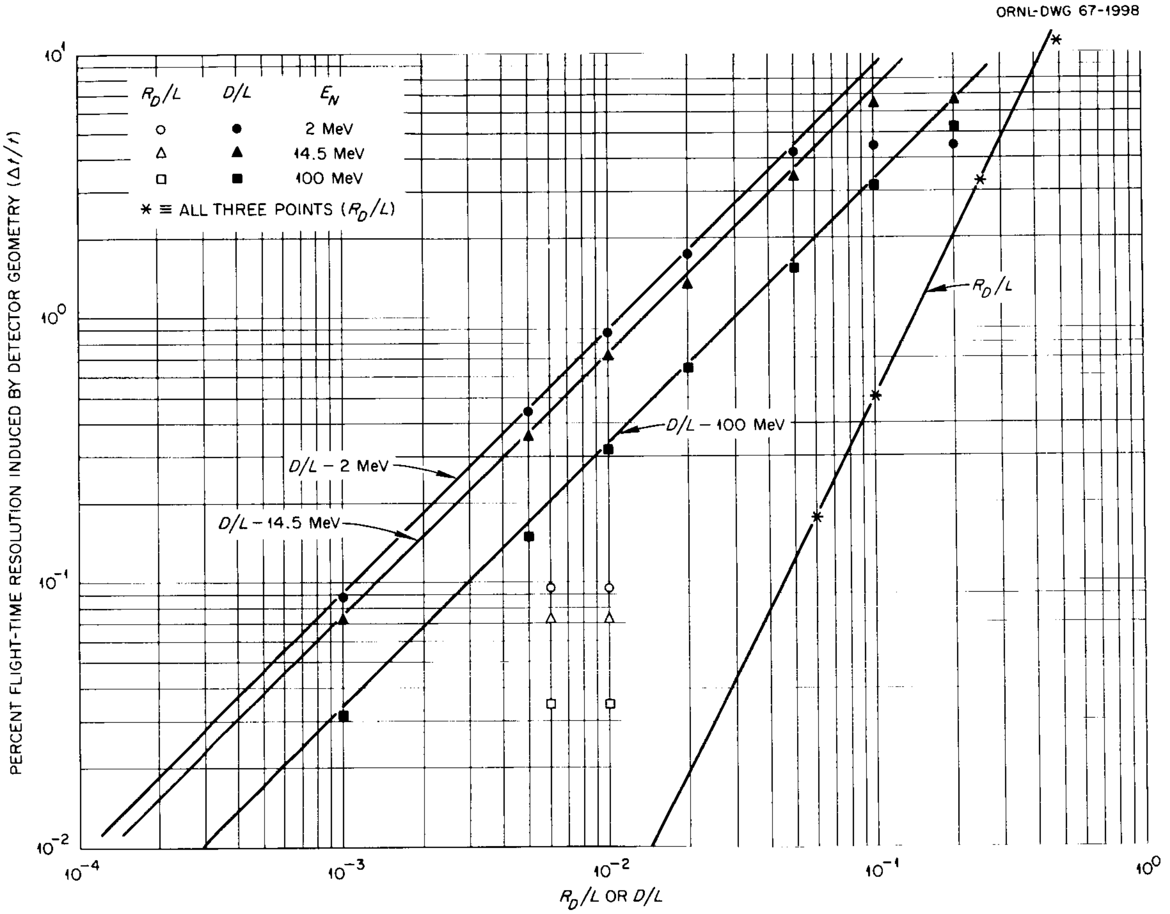

Figure 19. The flight-time resolution induced by detector geometry versus R_D/L and D/L for 2-, 14.5-, and 100-MeV.

Figure 20. For this case, the detector thickness is 10 cm. and the attenuation is of the order of $e^{-1.4}$ which produces the rapid drop off in the upper edge of the distribution.

When $2.35\ \sigma_j$ is small compared to the overall width of $C(v_p;v_n,t_i)$ the error introduced by quadratic subtraction does not seriously affect the final answer; about 0.25% for the case shown in Figure 20. For those cases where $10\% \leq 2.35\ \sigma_j/\mathrm{FWHM} \leq 37\%$, the effects of the jitter were removed using mathematical techniques proposed by Kalisz[45] to determine the resolving time of a coincidence circuit from empirical coincidence curves.

Provided the flight-time distribution is rectangular, we can write

$$\sigma_i^* = \sigma_i/\mathrm{FWHM} \qquad \text{VI-2}$$

where

σ_i = the standard deviation of the instrumental time jitter distribution,

FWHM = the full width at half maximum of the computed flight-time distribution.

Kalisz has tabulated the relationship between σ_i^* and τ^*, where $2(\mathrm{FWHM})\tau^*$ is the full width at half height of the true distribution corrected for the effects of smearing by a Gaussian distribution.

---

[45] Jósef Kalisz, A Method for Determination of the Resolving Time and Efficiency of the Coincidence Circuit on the Basis of a Single Empirical Delayed Coincidence Curve, Institute of Nuclear Research, Warsaw, Report INR No. 652/IA/PL, September 1965.

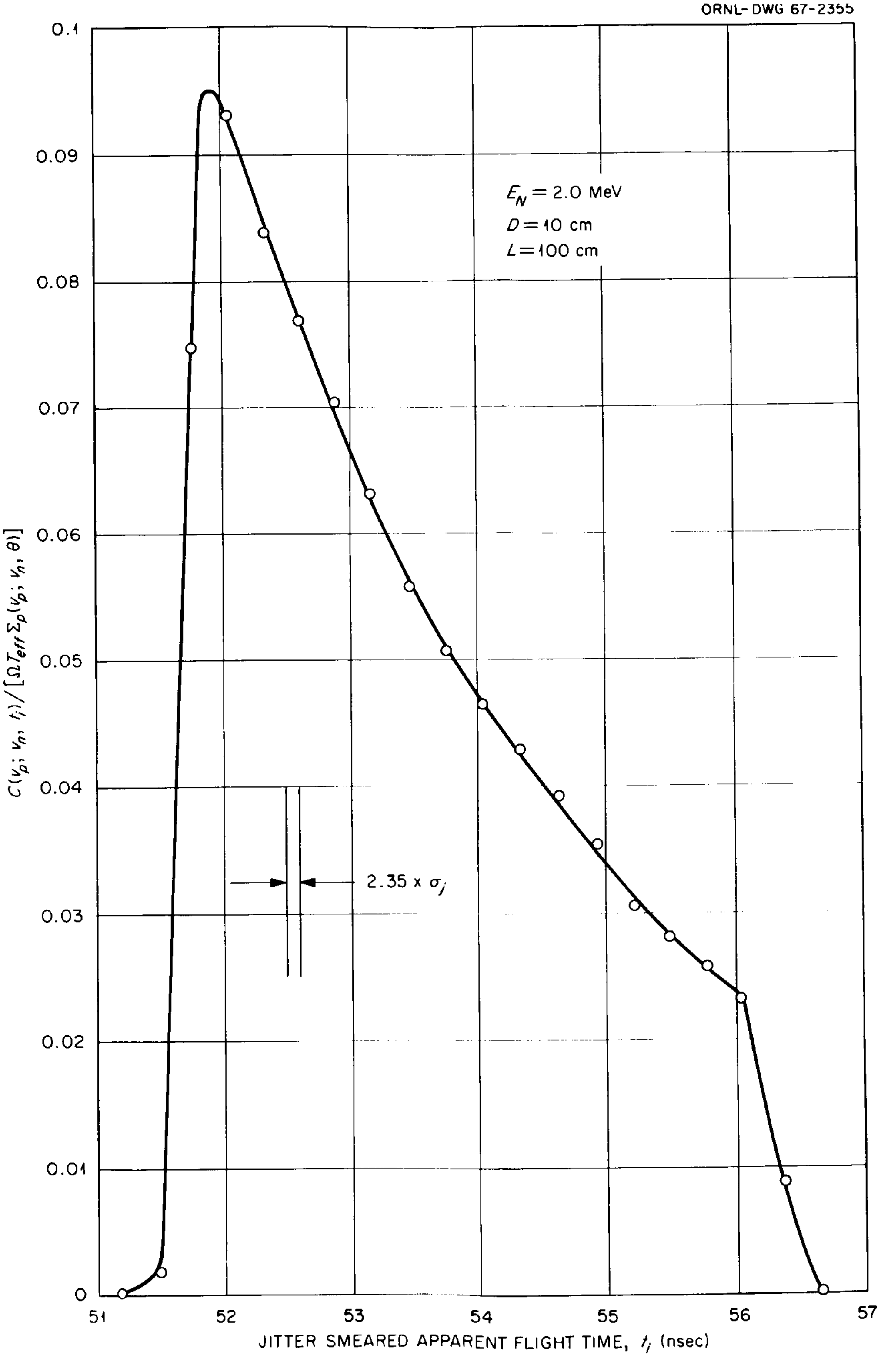

Figure 20. The physical flight-time distribution for the special case where D = 10-cm. and all other target and detector dimensions have been minimized. E_N = 2-MeV., L = 100-cm., and σ_j = 0.05 nsec.

If the value of $2.35\ \sigma_j$/FWHM > 35%, the data was usually not considered valid and the case was re-evaluated using a smaller value for σ_j.

We observe from Figure 19 that the computed values for the timing resolution, given by the data points, are in excellent agreement with the value predicted by the analytic expressions from Chapter III; the latter being given by the bold lines. For values of $D/L > 5 \times 10^{-2}$ we observe that the 2- and 14.5-MeV. points begin to drop away from the curve This apparent reduction in $(\Delta t/t)$ is due chiefly to the method of computing the FWHM of the distribution. In all cases the FWHM was defined conventionally and, as can be seen from Figure 20, the width is small compared to the total width of the distribution. For the thick detector cases in which the shape is heavily influenced by the effects of neutron attenuation, observation of the actual predicted time distribution indicates no real discrepancy with the maximum flight-time distributions.

The computed points for D/L fall slightly below the lines. This results since the lines were plotted using the equations derived in Chapter II in which the flight $(\Delta t/t)$ is defined in terms of $t = L/v_n$ where L is the normal distance from the origin of the target coordinate system to the face of the detector. The computed values for $(\Delta t/t)$ were obtained using the mean flight time.

Also plotted in Figure 19 is the flight-time resolution as a function of R_D/L. The agreement between the data is excellent in the region $R_D/L > 5 \times 10^{-2}$. Since the timing resolution is a function only of the radius and not the neutron energy, the points fall together as expected. As in the case of the detector thickness, the flight-time distribution is almost rectangular. There is, however, a fall off in the top of the distribution which is inversely proportional to the flight time. This behavior in the shape of the distribution is predicted by the analytic results when Equation IV-5 is integrated over all values of ℓ_f for a given flight time, t_i. This integration is performed asuming the target dimensions and detector thickness were negligible in extent.

When $R_D/L < 6 \times 10^{-2}$, the effects of the detector thickness used in the computation begin to dominate as shown by the open points.

Figure 21 shows the flight-time resolution induced by the target thickness plotted as a function of $T \sec\Psi/L$. The agreement between the computed values of $(\Delta t/t)$, given by the points, and those predicted using the equation shown in the figure is favorable. (The reader is referred to Section II, Chapter III for the detailed calculation leading to this equation.) As shown in the figure, some of the computed points have been corrected for the dominant detector contribution to the flight-time resolution by subtracting these effects in quadrature.

It is interesting to note the reversal in the expected flight-time resolution with increasing neutron energy. For this combination of target and detector angles ($\Psi = 30^\circ$ and $\theta = 60^\circ$), the extremum edges of the target can be used to approximate the maximum flight-time uncertainties for all neutron energies except for the particular case when $\cos 60^\circ = v_n/v_p$. For this energy, the maximum flight time must be approximated using Equation III-15 et seq.

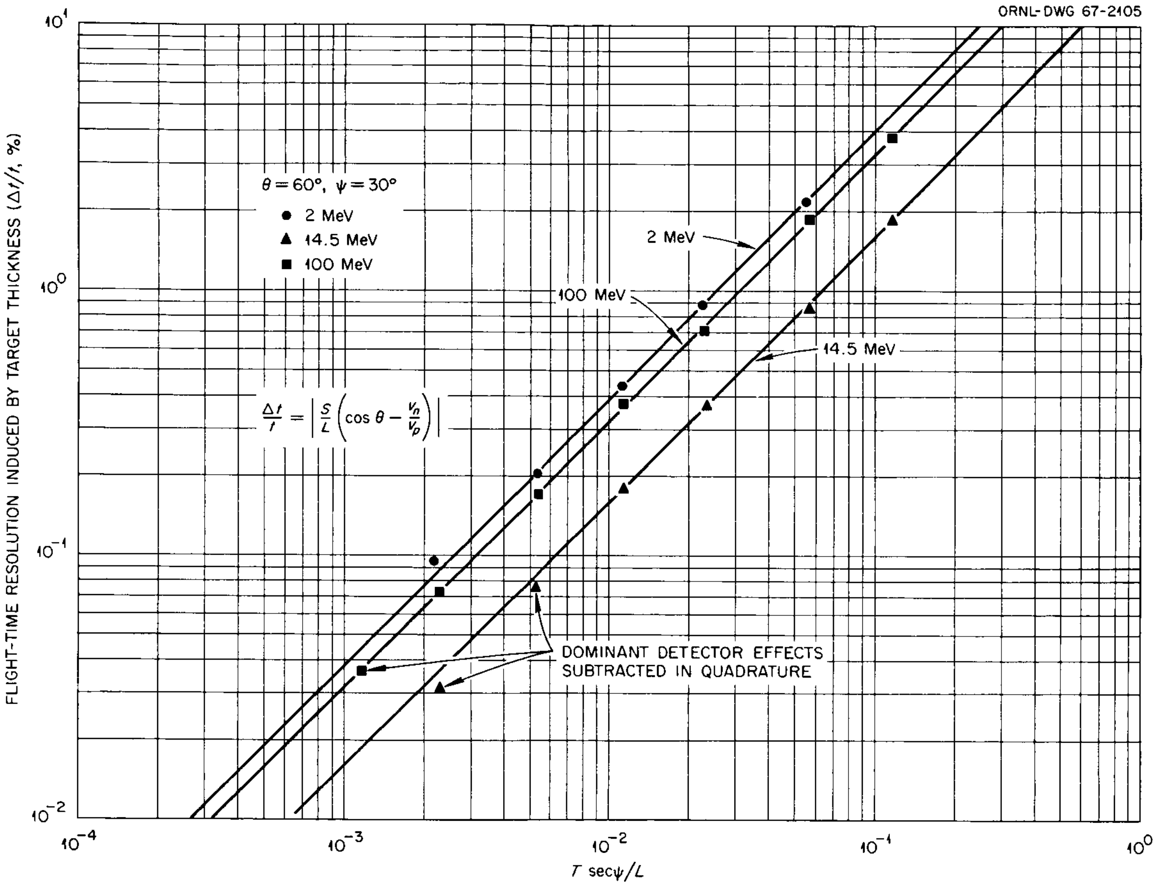

Figure 21. The flight-time resolution induced by target thickness versus T sec Ψ/L. For 2-, 14.5-, and 100-MeV. neutrons with $\theta = 60^\circ$ and $\Psi = 30^\circ$.

Figure 22 shows the shape of the computed distribution when $T \sec\Psi = 2.31$ cm., $L = 70$-cm., and $E_N = 2$ MeV. The time jitter comprises a significant portion of the total distribution. Since the distribution is rectangular, the effect of jitter may be removed using the Kalisz method. The FWHM is 0.433 nsec. and $\sigma_j = 0.1$ nsec. The resulting "geometric" distribution obtained using the Kalisz method 0.432 nsec., while subtraction of σ_j in quadrature yields 0.364 nsec.; about a 20% variation.

The comparison of the flight-time resolution is a function of the target radius requires a slightly different approach. In the derivation of the maximum flight-time uncertainties arising from the target radius, we assumed uniform beam density over the target radius. However, in deriving $C(v_p;v_n,t_i)$, we assumed that, in the absence of multiple scattering of the protons, the target radius corresponded to the radial dimension of the beam. The beam density was approximated by a Gaussian distribution in the x-z plane. In the numerical integration leading to $C(v_p;v_n,t_i)$, the limits for the y integral were defined by $y = \pm 2.5\sigma$, where σ is the standard deviation of the beam distribution.

To demonstrate the effects on the flight-time distribution of the target radius, we must introduce a different, but consistent, notation into the equations for leading to $(\Delta t/t)_{R_T}$ given in Chapter III.

The "radius" of the target was approximated by the FWHM of the beam distribution. Considering the rotation angle Ψ, the effective target radius was defined by

$$(R_T)_{\text{eff}} = 1.18\sigma \sec\Psi = \sigma_y' \quad . \qquad \text{VI-3}$$

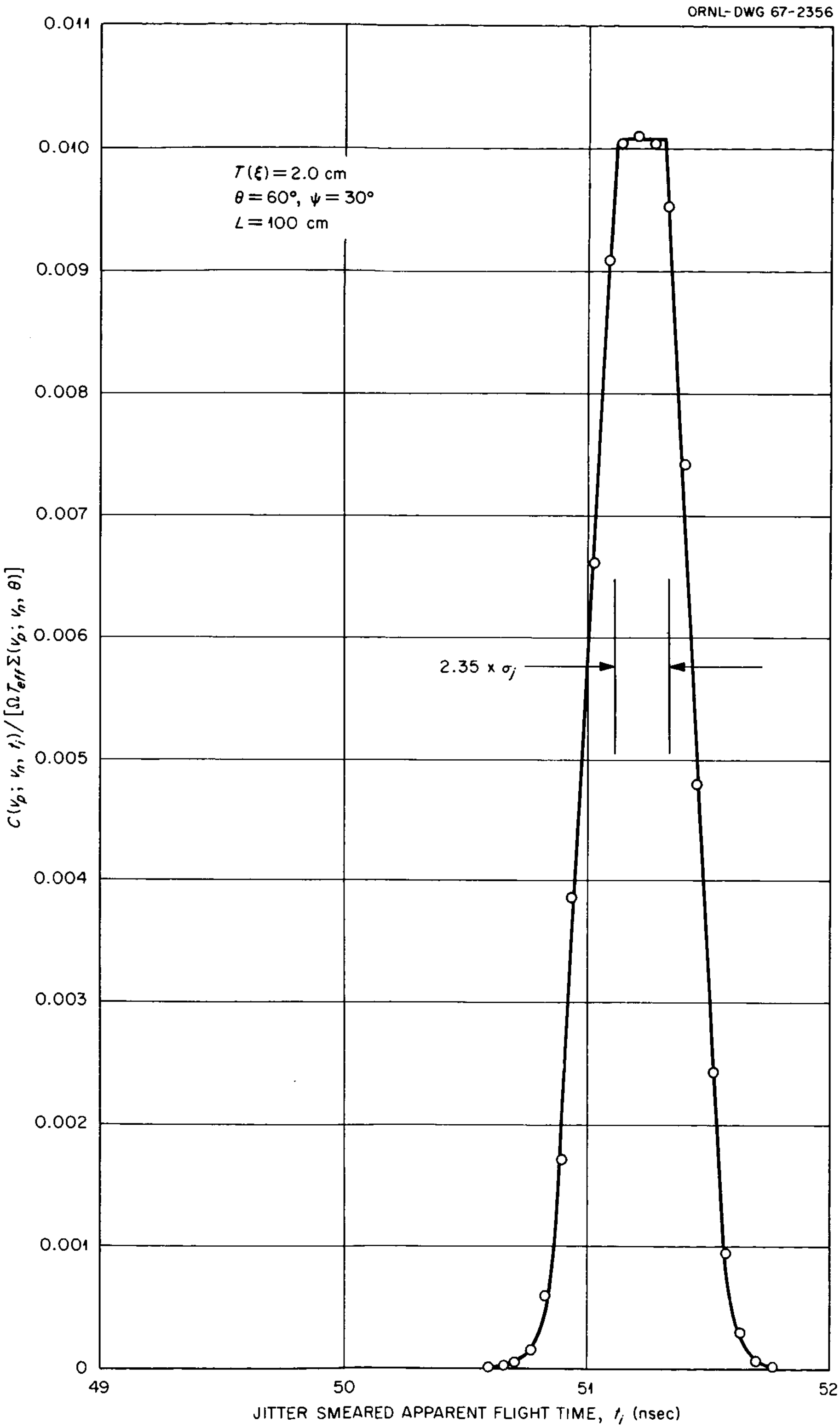

Figure 22. The physical flight-time distribution for the case where $T(\xi) = 2.0$ cm. and all other target and detector parameters have been minimized. For these data $E_N = 2.0$ MeV., $L = 100$ cm., $\theta = 60^\circ$, $\Psi = 30^\circ$, and $\sigma_j = 0.1$ nsec.

Equation III-20 may now be written with σ_y' replacing R_T.

Figure 23 shows the flight-time resolution as a function of σ_y'/L. The points give the computed values for $(\Delta t/t)$ obtained from the flight-time distribution while the lines were obtained using Equation III-20. For these cases, the instrumental jitter was subtracted in quadrature since the underlying "geometric" distribution is Gaussian.

In the numerical computation leading to Figure 23 the integration over the ρ coordinate of the detector was performed on the rear face of the detector. For the small detector used in these studies, the uncertainty in the final results due to the edge effects is negligible.

III. THE EFFECTS OF TIME SLEWING AND THE TIME-CHANNEL RESPONSE FUNCTION

Figure 24 shows the effects of the time slewing on the physical flight-time distribution for 14.5-MeV. neutrons obtained in Section I of this chapter. These data were obtained from Equation IV-38 using the time-slewing response function for 14.5-MeV. neutrons given in Figure 15.

Comparing the flight-time distribution from Figure 18 with these data, we observe significant broadening the original distribution in time with a corresponding truncation of the amplitude. The integral over the measured flight time t_m yields the efficiency of the detector obtained in Table IV.

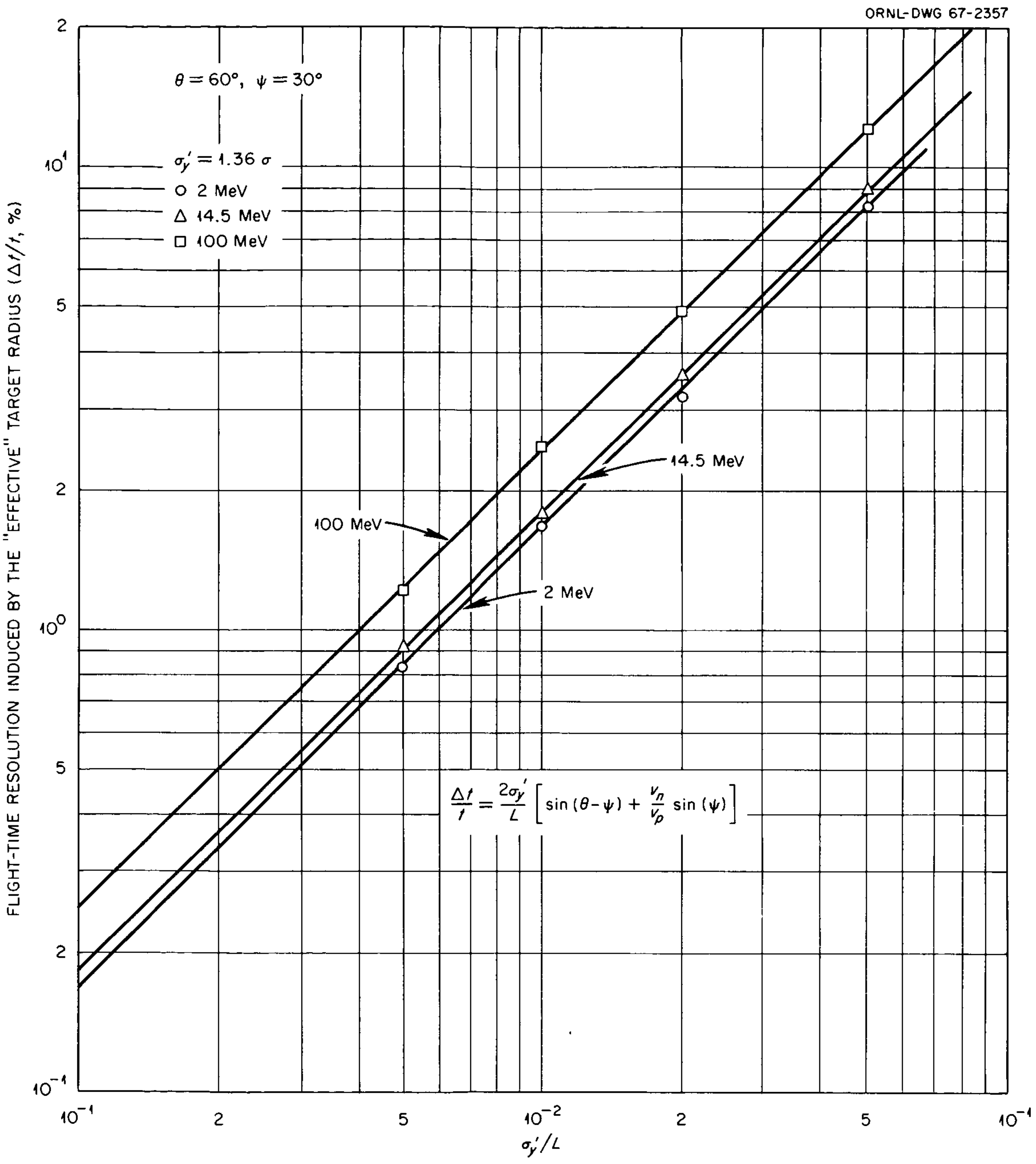

Figure 23. The flight-time resolution induced by the "effective" target radius versus σ_y'/L for 2-, 14.5-, and 100-MeV. neutrons. $\theta = 60^\circ$ and $\Psi = 30^\circ$.

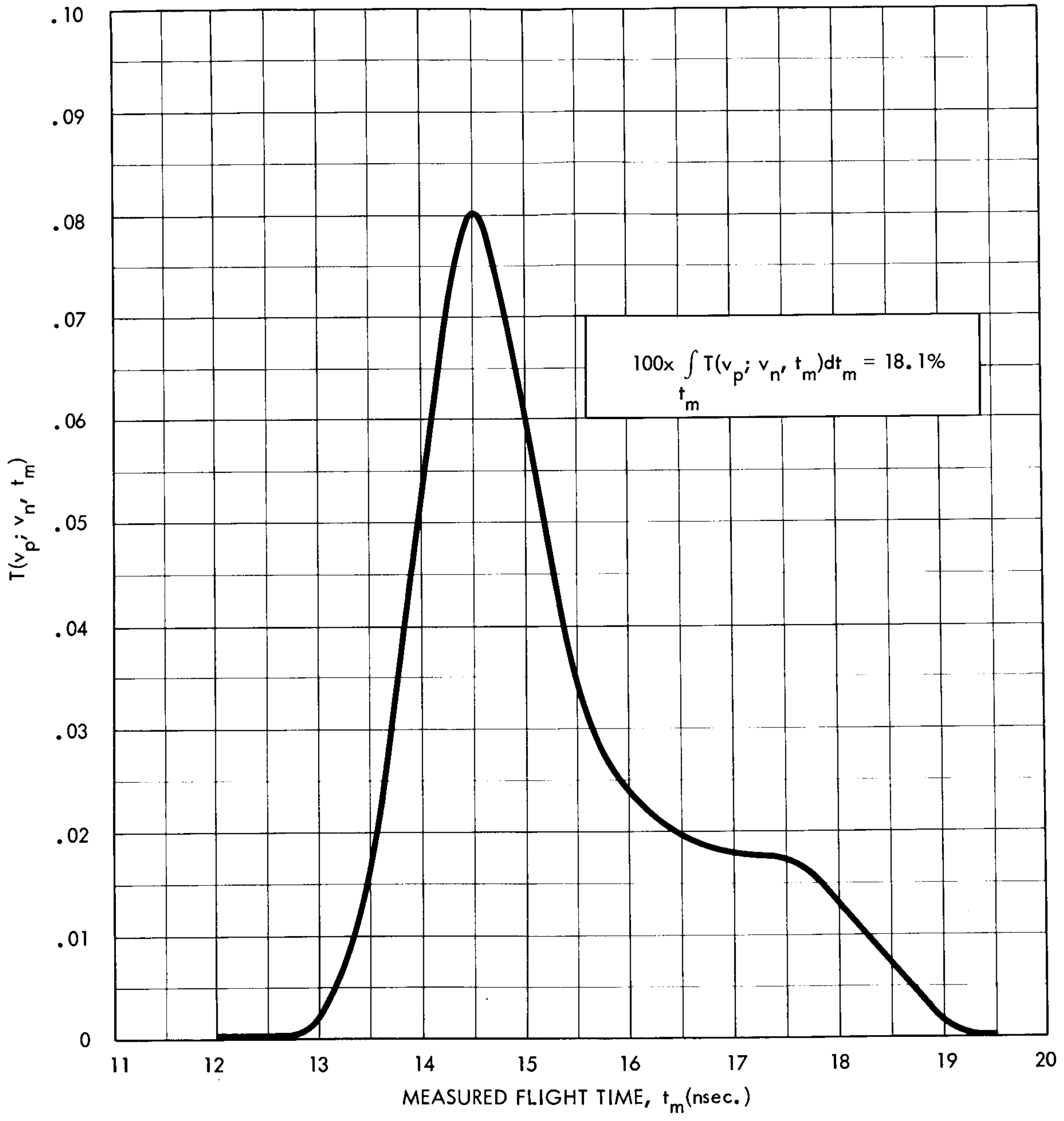

Figure 24. The probability per nsec. per incident proton per MeV. of neutron energy that a neutron has a measured flight time at t_m versus t_m, the measured flight time.

Figure 25 shows the time-channel response functions obtained from the slewing-smeared distribution in Figure 24. These response functions are obtained from Equation IV-37 using an analyzer calibration of 0.500 nsec./channel. The values obtained in this analysis are compared with the experimental points of Love _et al._[46] for approximately 14-MeV. neutrons at a flight path of 40 cm. The experimental data were normalized as well as possible for the differences in the flight path and the analyzer calibration.

---

[46] Love, op. cit., p. 22.

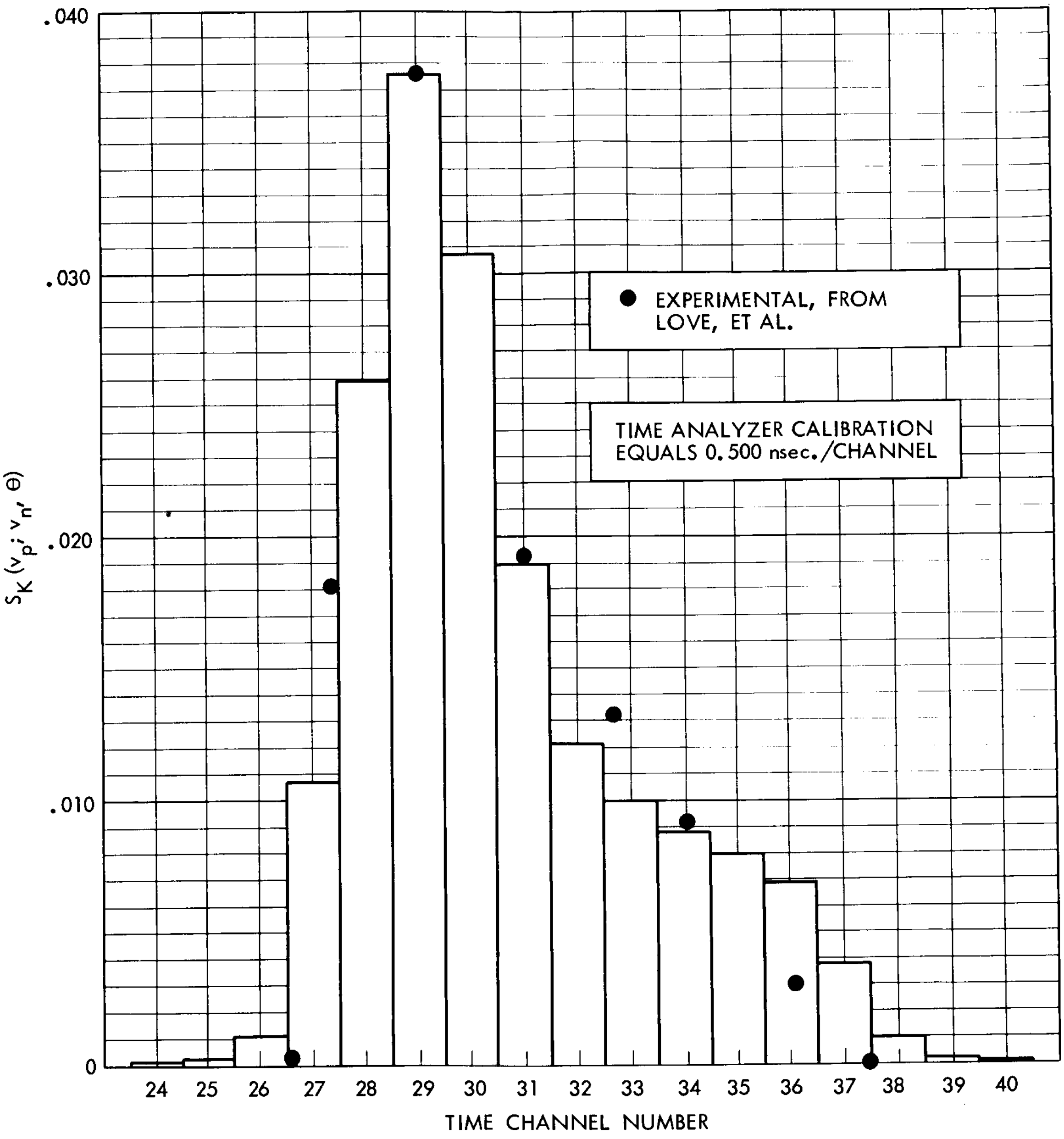

Figure 25. The time-channel response functions for 14.5-MeV. neutrons.

BIBLIOGRAPHY

BIBLIOGRAPHY

Adam, A., G. Palla, and P. Quittner, *Acta. Phys. Hung. Tom. XVII Fasc.* **3**, (1964).

Batchelor, R., *et al.*, *Nucl. Instr. Methods* **13**, 20 (1962).

Bertini, H., *Phys. Rev.* **131**, 1801 (1963).

Bertini, H., *Monte Carlo Calculations on Intranuclear Cascades*, ORNL-3383 (1963).

Birks, J. B., *IRE Transactions on Nuclear Science*, **NS-7**, 2 (1960).

Birks, J. B., *Proc. Phys. Soc.* **A64**, 74 (1952).

Bowen, P. H., *et al.*, *Nucl. Phys.* **30**, 457 (1962).

Brooks, F. D., *Proc. Symp. on Neutron Time-of-Flight Methods*, Saclay, (1961), p. 403.

Colombo, S., F. Gatti, and M. Pignanelli, *Nuovo Cimento* **5**, 1739 (1957).

Gammel, J. L., *Fast Neutron Physics*, Part II, (Interscience Publishers, New York, 1963).

Gatti, E., and V. Svelto, *Nucl. Instr. Methods* **30**, 213 (1964).

Grismore, R., and W. C. Parkinson, *Rev. Sci. Instr.* **28**, 245 (1957).

Kuo, Shan S., *Numerical Methods and Computers*, (Addison-Wesley, Reading, Massachusetts, 1965).

Kurz, R. J., *A 709/7090 Fortran II Program to Compute the Neutron Detection Efficiency of Plastic Scintillator for Neutron Energies from 1 to 300 MeV.*, UCRL-11339, March 1964.

Lanczos, Cornelius, *Applied Analysis*, (Prentice-Hall, Inc., Englewood Cliffs, New Jersey, 1956).

Love, T. A., *et al.*, *Absolute Efficiency Measurements of NE-213 Organic Phosphors for Detecting 14.4 and 2.6-MeV. Neutrons*, ORNL-3893 (1966).

Lundby, A., *Rev. Sci. Instr.* **22**, 324 (1951).

Neiler, J. H., and W. M. Good, Fast Neutron Physics, (Interscience Publishers, New York, 1963).

O'Neill, G. K., Phys. Rev. 95, 1235 (1954).

Peelle, R. W., et al., Differential Cross Sections for the Production of Protons in the Reactions of 160-MeV. Protons on Complex Nuclei, ORNL-3887 (1966).

Peelle, R. W., et al., Neutron Phys. Div. Ann. Progr. Rept., ORNL-3360 (1962).

Perey, F. G. J., Inelastic Scattering of 14-MeV. Neutrons in Carbon, Oxygen, and Lithium, Ph.D. dissertation, University of Montreal, (1960).

Putzulu, D. I., P. Aebersold, and W. R. Burrus, Description of the TERP System, A Fortran II/63, IV-63, 360 System for Efficient Interpolation, ORNL-TM-1706 (1966).

Rethneiv, J., et al., Nucl. Instr. Methods 17, 273 (1962).

Rybakov, B. V., and V. A. Siderov, Fast Neutron Spectroscopy, (Consultants Bureau, Inc., New York, 1960).

Santoro, R. T., A Fortran Program for Calculating the Time-Channel Response Function in Neutron Time-of-Flight Spectroscopy, to be published.

Schuttler, R. S., Efficiency of Organic Scintillators to Fast Neutrons, ORNL-3888 (1966).

Smith, R. V., Conference on Neutron Physics by Time-of-Flight, Gatlinburg, Tennessee (1956).

Verbinski, V. V., et al., The Response of Some Organic Scintillators to Fast Neutrons, Shielding Division Report, ANS-SD-2 (1964).

Voos, R. G. P., and R. Wilson, Proc. Roy. Soc. (London) A236, 41 (1956).

APPENDICES

APPENDIX A

CALCULATION OF t_p: THE INTERVAL FROM TIME ZERO TO THE (p,n) INTERACTION IN THE TARGET

The time spent by the proton in the target is given by the relation

$$t_p = \int_{\ell_p} \frac{dx}{v_p(x)} + t_e \qquad \text{A-1}$$

where

dx = the incremental distance travelled by the proton in the target,

$v_p(x)$ = the proton velocity at the distance x in the target, and

t_e = the time required for the proton to travel from the plane passing through $x = 0$ to the entrance face of the target at velocity v_p. (t_e is usually a negative number.)

The proton loses energy in the target through numerous atomic collisions. Its flight time through the target is a function of the incremental energy loss per cm., dE/dx. In the nonrelativistic approximation, the proton energy is given by the familiar equation $E_p = (1/2)\, mv_p^2$. Differentiating with respect to x we obtain

$$(-dE/dx) = mv_p\ (-dv_p/dx)\ . \qquad \text{A-2}$$

(-dE/dx) is a positive number; the minus implying a decrease in energy with increasing x. Expanding $v_p^{-1}(x)$ in a Taylor series gives

$$v_p^{-1}(x) = v_p^{-1}(0) - (v_p^{-2}\ x)\ (dv_p/dx) + \dots \quad . \qquad \text{A-3}$$

Substituting dv_p/dx from Equation A-2 into A-3 and introducing the result into Equation A-1 gives

$$t_p = \int_0^{\ell_p} \frac{dx}{v_p} + \frac{dx}{mv_p^3}\,(-dE/dx) \int_0^{\ell_p} x\,dx + t_e \quad . \qquad \text{A-4}$$

ℓ_p is the proton penetration depth prior to the (p-n) interaction given by Equation II-3. Noting that $mv_p^3 = 2v_pE_p$ and completing the integration, we obtain the result

$$t_p = \frac{\ell_p}{v_p} + \frac{\ell_p^2}{4v_pE_p}\,(-dE/dx) + t_e \quad . \qquad \text{A-5}$$

The convention was adopted that the zero of time for a proton is at the instant it would have passed through the plane x = 0 if the target were absent. Then,

$$t_e = \frac{x - \ell_p}{v_p} \quad . \qquad \text{A-6}$$

Substituting this result into Equation A-5 yields

$$t_p \cong \frac{x}{v_p} + \frac{\ell_p^2}{4v_pE_p}(-dE/dx) \quad . \qquad \text{A-7}$$

APPENDIX B

CALCULATION OF $(\hat{i}' \cdot \hat{\Omega})$, ℓ_f, AND ℓ_T

The quantities $(\hat{i}' \cdot \hat{\Omega})$, ℓ_f, and ℓ_T introduced in Chapter IV in the analysis leading to the physical flight-time distribution of detected neutrons will be derived here in terms of the known quantities L, x, y, y', z', θ, Ψ, τ_1, and τ_2.

I. THE DERIVATION OF ℓ_f and $(\hat{i}' \cdot \hat{\Omega})$

The distance travelled by the neutron from its birth point in the target to the face of the detector is ℓ_f. Introducing $\tilde{x}$ and $\tilde{y}$, the target interaction coordinates in a coordinate system rotated through an angle θ in the x-y plane,

$$\begin{aligned} \tilde{x} &= x \cos\theta + y \sin\theta \\ \tilde{y} &= y \cos\theta - x \sin\theta \end{aligned} , \qquad \text{B-1}$$

we can write the cartesian components of $\vec{\Omega}$ in the rotated coordinate system as

$$\begin{aligned} \Omega_{x'} &= L - \tilde{x} \\ \Omega_{y'} &= y' - \tilde{y} \\ \Omega_{z'} &= z' \end{aligned} , \qquad \text{B-2}$$

if we make the identification

$$|\vec{\Omega}| = \ell_f \quad .$$

It follows from the Pythagorean Theorem that

$$\ell_f = \sqrt{(L - \tilde{x})^2 + (y' - \tilde{y})^2 + (z')^2} \quad . \qquad \text{B-3}$$

$(\hat{i}' \cdot \hat{\Omega})$ is the cosine of the direction angle of $\hat{\Omega}$ relative to the x′-coordinate system. From B-2,

$$(\hat{i}' \cdot \hat{\Omega}) = \frac{\hat{i}' \cdot \vec{\Omega}}{\ell_f} = \frac{L - \tilde{x}}{\ell_f} \quad . \qquad \text{B-4}$$

It can be shown from similar arguments

$$\begin{aligned} (\hat{j}' \cdot \hat{\Omega}) &= \frac{\hat{j}' \cdot \vec{\Omega}}{\ell_f} = \frac{y' - \tilde{y}}{\ell_f} \\ (\hat{k}' \cdot \hat{\Omega}) &= \frac{\hat{k}' \cdot \vec{\Omega}}{\ell_f} = \frac{z'}{\ell_f} \end{aligned} \quad . \qquad \text{B-5}$$

II. DERIVATION OF ℓ_T, the PATHLENGTH OF THE SECONDARY NEUTRON IN THE TARGET

The length of ℓ_T is dependent on the target-detector orientation and separate calculations are required for the target in transmission, $|\theta - \Psi| \leq \pi/2$, and in reflection $|\theta - \Psi| > \pi/2$.

The Target in Transmission

Neutrons born in the target at P_T are emitted at an angle Θ with respect to the proton beam axis. ℓ_T is obtained from the normal equation of the plane of the exit face of the target. According to this equation,

$$\ell_T \cos\varphi = |ON| \qquad \text{B-6}$$

where $\overrightarrow{ON}$ is the normal from P_T to the exit face and φ is the angle between $\overrightarrow{ON}$ and $\hat{\Omega}$. The length of ON is

$$|ON| = \tau_2 - x \cos\Psi - y \sin\Psi \quad . \qquad \text{B-7}$$

$\cos\varphi$ is obtained from the equation

$$\cos\varphi = \cos\alpha_1 \cos\alpha_2 + \cos\beta_1 \cos\beta_2 + \cos\gamma_1 \cos\gamma_2 \qquad \text{B-8}$$

where $(\alpha_1 \beta_1 \gamma_1)$ are the direction angles of ℓ_T and $(\alpha_2 \beta_2 \gamma_2)$ those of $\overrightarrow{ON}$; all angles being measured relative to $(x'y'z')$ along the direction $\hat{\Omega}$

its direction cosines are given by Equations B-4 and B-5. The direction cosines for $\overrightarrow{ON}$ are given by

$$\begin{aligned} \cos\alpha_1 &= \widehat{ON} \cdot \hat{i}' = \cos(\Psi - \theta) \\ \cos\beta_1 &= \widehat{ON} \cdot \hat{j}' = \sin(\Psi - \theta) \\ \cos\gamma_1 &= \widehat{ON} \cdot \hat{k}' = 0 \end{aligned} \qquad \text{B-9}$$

where $\widehat{ON}$ is the unit vector along $\overrightarrow{ON}$. $\widehat{ON} \cdot \hat{k}' = 0$ since ON is constrained to the x-y plane. Then Equation B-6 can be written

$$\ell_T = \frac{(\tau_2 \sec\Psi - x - y \tan\Psi) \cos\Psi}{\left[\frac{L - \tilde{x}}{\ell_f} \cos(\theta - \Psi) - \frac{y' - \tilde{y}}{\ell_f} \sin(\theta - \Psi)\right]} \qquad \text{B-10}$$

which gives the magnitude of ℓ_T for the target in transmission.

Target in Reflection

When $|\theta - \Psi| > \pi/2$, the derivation for ℓ_T follows the same procedure. In this case, $|ON|$ is given by $\ell_P \cos\Psi$ where ℓ_p is given by Equation II-3. Then,

$$\ell_T = \frac{(x + y \tan\Psi - \tau_1 \sec\Psi) \cos\Psi}{\left[\frac{L - \tilde{x}}{\ell_f} \cos(\theta - \Psi) - \frac{y' - \tilde{y}}{\ell_f} \sin(\theta - \Psi)\right]} \qquad \text{B-11}$$

for the target in reflection.

ORNL-4114
UC-34 — Physics

INTERNAL DISTRIBUTION

1. Biology Library
2-4. Central Research Library
5-6. ORNL — Y-12 Technical Library
Document Reference Section
7-262. Laboratory Records Department
263. Laboratory Records, ORNL R.C.
264. L. S. Abbott
265. H. W. Bertini
266. R. Burrus
267. G. DeSaussure
268. C. D. Goodman
269. C. E. Larson
270. H. G. MacPherson
271. F. C. Maienschein
272. R. W. Peelle
273. R. T. Santoro
274. M. J. Skinner
275. D. R. Vondy
276. A. M. Weinberg
277. G. Dessauer (consultant)
278. B. C. Diven (consultant)
279. M. H. Kalos (consultant)
280. L. V. Spencer (consultant)

EXTERNAL DISTRIBUTION

281. J. A. Swartout, Union Carbide Corporation, New York
282. P. B. Hemmig, Division of Reactor Development and Technology,
U.S. Atomic Energy Commission, Washington, D.C. 20545
283. I. F. Zartman, Division of Reactor Development and Technology,
U.S. Atomic Energy Commission, Washington, D.C. 20545
284. Research and Development Division, AEC, ORO
285-605. Given distribution as shown in TID-4500 under Physics category
(25 copies — CFSTI)